Journal of Hazardous Materials Advances 21 (2026) 100951

Contents lists available at ScienceDirect

Journal of Hazardous Materials Advances

journal homepage: www.elsevier.com/locate/hazadv

Biochar derived from spent mushroom substrate for efficient atrazine removal in aqueous solution

Yuhang Sun [a,b,1], Ping Han [b,1], Jing Li [b,c], Qi Gao [b], Mingyu Zhao [c,d], Kai Wang [c], Zhan Wang [a], Ercheng Zhao [b], Hongtao Zou [a,*], Junxue Wu [b,*]

[a] College of Land and Environment, Shenyang Agricultural University, Shenyang 110866, China
[b] Institute of Plant Protection, Beijing Academy of Agriculture and Forestry Sciences, Beijing 100097, China
[c] College of Resources and Environmental Sciences, China Agricultural University, Beijing 100193, China
[d] Soil Physics and Land Management Group, Wageningen University & Research, 6700 AA Wageningen, , Netherlands

ARTICLE INFO

Keywords:
Atrazine
Adsorption
Biochar
Mechanisms
Spent mushroom substrate

ABSTRACT

Given its extensive global usage and environmental persistence conferred by the stable triazine ring structure, the frequent detection of atrazine (ATZ) in the environment poses ecological and health risks. Spent mushroom substrate (SMS), as a widely available and low-cost agricultural waste, and its lignocellulosic composition and inherent porosity are conducive to generating highly aromatic and porous biochar structures for adsorbing ATZ. This study pioneeringly prepared biochar (BC) and acid-treated BC derived from SMSs of *Pleurotus ostreatus*, *Oudemansiella apalosarca*, and *Lentinula edodes*) via pyrolysis at 800 °C. Comprehensive characterization confirmed that the physicochemical properties of BC were significantly influenced by feedstock origin and acid treatment. Acid treatment improved specific surface area, porosity, and aromaticity, and alongside reduced hydrophilic ash content. Batch experiments indicated that acid-treated BC improved ATZ adsorption efficiency with removal rates increasing by 3.5–5.6 times, following the order of APBC (98.2 %) > AOBC (38.4 %) > ALBC (27.1 %). Adsorption kinetics and isotherms indicated heterogeneous surface interactions and multi-mechanism involvement. The elevated logK_{OC} values of acid-treated BC reflected stronger affinity for ATZ on organic carbon-enriched sites. Mechanistic analysis quantified four dominant pathways with distinct contribution ranges of pore filling (2.2–42.4 %), hydrophobic partitioning (2.2–47.2 %), π–π electron donor-acceptor interactions (15.6–49.8 %), and hydrogen bonding (0.9–35.0 %). Thermodynamic studies revealed spontaneous, endothermic, and entropy-driven adsorption processes, and adsorption capacity of ATZ was favored under acidic and high-temperature conditions. These findings not only offer a solution for agricultural byproducts SMSs reuse into high-efficiency adsorbents through pyrolysis and acid modification but also establish a method to mitigate pesticide contamination in aqueous systems.

1. Introduction

Atrazine (ATZ, 6-chloro-N2-ethyl-N4-isopropyl-1,3,5-triazine-2,4-diamine), a triazine-class herbicide characterized by persistent residual activity, is extensively employed for pre- and post-emergent weed control in dryland cropping systems with annual global consumption of 70,000–90,000 tons (Hu et al., 2023). The structure stability of ATZ's triazine ring confers high environmental persistence and resistance to biodegradation, resulting in ubiquitous contamination across ecosystems (Turan et al., 2022; Raluca et al., 2023). With a good water solubility and soil organic carbon-water partitioning coefficient, ATZ exhibits significant mobility, leading to detectable residues in soil (up to 1100 mg/kg), surface water (up to 3.45 mg/L), and ground water (up to 4 mg/L) (Zhang et al., 2023). Such concentrations exceed international regulatory thresholds by 3–4 orders of magnitude (1.0 mg/kg in soil and 0.1–3 μg/L in water), posing critical challenges. Residues of ATZ in the soil can also cause phytotoxicity to subsequent crops such as wheat and soybeans, reducing agricultural production yields by 15–40 %. Meanwhile, ATZ also poses potential risks to non-target organisms and human beings by affecting the endocrine, central nervous system and immune

* Corresponding authors.
E-mail addresses: zht@syau.edu.cn (H. Zou), wujunxue@baafs.net.cn (J. Wu).
[1] The first two coauthors contributed to the manuscript equally and shall be considered as co-first authors.

https://doi.org/10.1016/j.hazadv.2025.100951
Received 12 October 2025; Received in revised form 11 November 2025; Accepted 21 November 2025
Available online 21 November 2025

system (He et al., 2023; Wang et al., 2022).

At present, ATZ contamination remains a persistent global environmental challenge. Despite its environmental behaviors such as adsorption, migration, and metabolic transformation have been extensively studied (Chang et al., 2022), the key technology for addressing ATZ pollutants is remediation (He et al., 2019; Chang et al., 2022). Current remediation approaches encompass biochar (BC) amendments (Jin et al., 2016; Lima et al., 2022; Wang et al., 2022), microbial degradation (Tappin et al., 2012), BC-mediated functional bacterial biofilm (Zhang et al., 2024), BC-functional microorganisms (Tao et al., 2020), electrokinetic-assisted phytoremediation (Sanchez et al., 2019, 2020), gamma-ray irradiation (Wang et al., 2012), photo-electrochemistry (van der Zalm et al., 2023; Yasar, 2024), ozonation (Soltysova et al., 2023), and activated persulfate (Zhang et al., 2023; Li et al., 2024; Liang et al., 2024). Chemical remediation risks secondary contamination from persistent reagents or toxic byproducts, alters soil properties impairing ecological function, and faces scalability challenges due to high costs. Although microbial remediation is low-cost, when confronted with complex environmental conditions, the bioavailability of pollutants is limited, and the degradation of refractory compounds is slow or stagnant. BC-enhanced adsorption has emerged as a prominent solution due to its exceptional adsorption capacity, cost-effectiveness and environmental compatibility. Sorption efficiency of ATZ in aqueous solution onto wood-based BC achieving 41.6 %−100 % (Lima et al., 2022). Adsorption capacities of ATZ were in the range of 0.6–0.8 mg/g, 1.0–1.2 mg/g, 2.5–3.0 mg/g by the BC, acid-treated BC, and montmorillonite-BC driven from peanut shell with 600 °C pyrolysis, respectively (Wang et al. 2020; Wang et al., 2022). It indicates that the potential of BC for adsorption of ATZ in the environment.

BC is a carbonaceous solid material synthesized via pyrolysis of biomass under oxygen-limited conditions(Dong et al., 2024), and its raw materials come from a wide range of sources, including but are not limited to the following: agricultural residue (i.e., animal manure, sawdust, crop straw, etc.), forestry byproducts (i.e., hardwood and softwood), and urban waste (i.e., sewage sludge, food processing residues). The physiochemical properties of BC such as specific surface area, pore architecture, and surface functionality are governed by feedstock composition and pyrolysis parameters(Yavari et al., 2015). The expansion of microporosity and surface area, as well as the increase in carbon content and hydrophobicity of BC, typically occur with a rise in pyrolysis peak temperature (Yavari et al., 2015). Therefore, high pyrolysis treatment temperature (e.g., >500 °C) is often used to prepare the BC expected to have a good adsorption efficiency for the pollutants (Wang et al., 2020).

The development of novel biomass feedstocks for BC production has emerged as a pivotal research frontier in contaminant remediation, driven by demands for sustainable resource utilization and circular economy integration. Spent mushroom substrate (SMS), a lignocellulose-rich byproduct of fungal cultivation, represents an underutilized yet promising precursor for engineered BC synthesis. China, contributing 70 % of global edible mushroom production, generated 41 million tons of SMS in 2020, with an estimated yield ratio of 5 kg SMS per 1 kg harvested mushrooms (Guo et al., 2022; Leite Vieira et al., 2022). Compositional Profile of SMS include 98–99 wt % of agricultural/forestry residues (straw, sawdust, cottonseed hulls, rice husks, poultry manure) and 1–2 wt % of mineral auxiliary materials (calcium carbonate, gypsum, etc.). Current disposal practices predominantly involve discarding, landfilling or uncontrolled incineration, which has potential risks of eutrophication via nitrate/phosphate leaching, antibiotic resistance gene dissemination from residual mycelia, and greenhouse gas emissions. From the perspective of utilizing agricultural waste resources, compared with traditional BC feedstocks (e.g., straw, sludge), SMS offers distinct advantages for pollutant adsorption, notably higher lignocellulose content and a more favorable pore structure. Especially, the fungal mycelium acts as a natural engineer, pre-digesting the lignocellulose to create a superior porous template, leading to biochar with inherently higher surface area and pore volume. In addition, it transforms a major agricultural waste problem into a high-value resource, promoting sustainable waste management and reducing environmental footprint. As a low-cost and abundant by-product, it improves the economic feasibility of large-scale biochar production. These inherent properties make SMS a strategically superior feedstock compared to raw biomass. Fow now, the SMS has been reported as biosorbents for metals (Wang et al., 2019) and persistent organic micropollutants (Ghose and Mitra, 2022) and even for preparation BC as adsorbents of dye (Sewu et al., 2017; Han et al., 2023), endocrine disruptors (Leite Vieira et al., 2022), etc. However, the BC driven by SMS for pesticide remediation has been rarely reported.

Post-synthesis modifications can further optimize adsorption performance. The BC adsorption capability can be improved by P-doped BC (Suo et al., 2019), iron-modified BC (Chen et al., 2023, 2024), in situ boron-doped cellulose-based BC (Wang et al., 2023), layered double hydroxides modified sludge BC (Zheng et al., 2022), bentonite clays modified BC (Ajala et al., 2018), nano-MgO modified fallen leaf BC (Cao et al., 2021), etc. In addition, acid treatment can increase the organic carbon content, surface area, and pore volume of BC (Singh et al., 2022; Zhang et al., 2018). Considering that the SMSs contain ash content, acid treatment modification might be one suitable method. Adsorption performance of BC was influenced by environmental factors such as temperature, pH value, and ions (Gao et al., 2023). The reported adsorption mechanisms of organic pollutants on the BC generally involve physical adsorption (i.e., hydrophobic partition, pore confinement, π-π electron donor-acceptor (EDA) interactions), and chemical adsorption (i.e., hydrogen bonding, covalent bonding with O/N-functional groups) (Wang et al., 2020; Gao et al., 2023).

The objectives of our work were to prepare and characterize the BC using three different SMSs (*Pleurotus ostreatus, Oudemansiella apalosarca*, and *Lentinula edodes*), to illustrate effects of SMS type and acid treatment on the ATZ sorption, analysis of adsorption kinetics and adsorption isotherms of ATZ, effects of solution pH, inorganic salt and humic acid (HA), and to reveal the adsorption mechanisms of ATZ on the BC.

2. Materials and methods

2.1. Materials

ATZ standard (98 % purity) was obtained from J&K Scientific Ltd., China. Chromatographically grade acetonitrile (ACN) was obtained from Dikma Technologies Inc, China. Analytical grade sodium chloride (NaCl), sodium bicarbonate ($NaHCO_3$), calcium chloride ($CaCl_2$), humic acid (HA), sodium hydroxide (NaOH), and hydrochloric acid (HCl) were obtained from Sinopharm Chemical Reagent Co. Ltd., China. Ultrapure water was prepared with a Master system (Master-S30UV, Shanghai Hetai Instrument Co. Ltd., China). Three SMSs of *pleurotus ostreatus, oudemansiella apalosarca*, and *lentinula edodes* were sourced from Edible Fungi Lab in Institute of Plant Protection, Beijing Academy of Agriculture and Forestry Sciences. Compositions of three SMSs are detailed in *Table S1*.

2.2. Preparation and characterization of BC

The SMSs were air-dried naturally for two weeks, ground into a powder, and passed through a 60-mesh sieve (< 0.25 mm). The powdered SMS was transferred to a quartz boat and then subjected to pyrolytic carbonization in a horizontal tube reactor (SG-GL 1200 K, Shanghai Daheng Optical Precision Machinery Co. Ltd., China) under N_2 protection with a flow of 5 L/h. The pyrolytic process comprised three sequential phases: ramp-up stage, 10 °C/min from ambient to 800 °C; isothermal stage, maintained 800 °C for 1 h; natural cooling under inert atmosphere until<80 °C. The prepared untreated BC using the waste substrate of *pleurotus ostreatus, oudemansiella apalosarca*, and *lentinula edodes* were named PBC, OBC, and LBC, respectively. Following the

initial treatment, the samples underwent sequential purification through 24 h oscillation wash cycles with 1 M HCl solution (solid-to-liquid ratio = 1:20) at 180 rpm at 25 °C. After three acid treatments, the solid product was separated from the acid solution by centrifugation at 8000 rpm for 10 min. The supernatant was decanted. The resulting acid-washed BC was then rinsed with deionized water and centrifuged repeatedly until the supernatant reached a neutral pH (pH = 6.5 - 7.5). The purified BC was dried in an oven at 60 °C for 12 h until a constant weight was achieved. Prepared acid deashing PBC, OBC and LBC were named APBC, AOBC, and ALBC, respectively. The dried APBC, AOBC, and ALBC were ground, passed through a 100-mesh sieve, and stored in a sealed container for subsequent experiments.

Comprehensive characterizations of the prepared BC were conducted through multi-analytical techniques to elucidate structural and physicochemical properties governing organic pollutant remediation. Microstructural features and elemental spatial distribution were analyzed using scanning electron microscopy (SEM, Tescan Mira LMS, Czech) with energy-dispersive X-ray spectroscopy (EDS, Xplore, Oxford Instrument Tech. Co. Ltd., United Kingdom) operating at 10 kV acceleration voltage. Specific surface area and pore size distribution were quantified via Brunauer-Emmett-Teller (BET) analysis of N_2 adsorption-desorption isotherms (Micromeritics ASAP 2460, McMurray Tik Instrument Co. Ltd., USA). Surface functional groups were screened by Fourier-transform infrared spectroscopy (FTIR, Thermo Scientific Nicolet iS5. Symefeishier Tech. Co., USA) across 400–4000 cm^{-1} (resolution: 4 cm^{-1}; 64 scans), with peak assignments referencing the BC functional group index. Elemental composition and chemical bonding states were identified using X-ray photoelectron spectrometry (XPS, Thermo Scientific K-Alpha, Symefeishier Tech. Co., USA) with Al Kα radiation. Bulk elemental analysis of carbon, hydrogen, nitrogen, and sulfur (CHNS) content was performed by combustion at 1150 °C (Elementar Unicube, Element Elementar, Germany), with oxygen content determined by mass balance. Surface charge properties were assessed through zeta potential measurements via dynamic light scattering (DLS, Malvern Zetasizer Nano ZS90, Malvern Instruments UK Limited, United Kingdom).

2.3. Adsorption experiments

The ATZ adsorption experiments on the BC were conducted by batch methods (Wang et al., 2024). 25 mg of the BC was transferred into a 50 mL conical flask containing 25 mL of 10 mg/L ATZ and 0.01 M $CaCl_2$ solution. The flask was placed in a water bath shaker with an oscillation rate of 180 rpm at 25 °C for 24 h. The supernatant sample was centrifugated at 10,000 rpm for 1 min and filtered into a vial using 0.22 μm PES membrane. Control treatments with only BC or ATZ solution addition were set up.

Firstly, the effects of SMS type and acid treatment on the ATZ adsorption were investigated. Secondly, adsorption kinetics and adsorption isotherms of ATZ were also conducted using the same experimental conditions as above. The adsorption kinetic tests of ATZ were set as an initial ATZ concentration of 10 mg/L, a BC dosage of 25 mg, and sampling times of 0.5, 1, 2, 4, 8, 12, and 24 h. The adsorption isotherm tests of ATZ were conducted with an initial ATZ concentration of 1, 2, 5, 10, 15, and 20 mg/L, the BC dosage of 25 mg, and sampling time of 24 h. Thirdly, the effects of solution temperatures (25 °C, 35 °C and 45 °C), solution pH (2.9, 4.4, 6.5, 7.5, 8.9, and 10.5), inorganic salt (1, 10, and 100 mM of NaCl and $NaHCO_3$), and HA (1 and 10 mg/L) on ATZ adsorption was carried out by adding corresponding salt or HA in the initial 25 mL of 10 mg/L ATZ solution conditions. The initial pH values of the solution were adjusted using 1 M HCl and NaOH solution. Each treatment was conducted in triplicate. Control treatment of inorganic salt and HA effect experiment was conducted without corresponding NaCl, $NaHCO_3$, and HA.

2.4. Analytical methods

Concentrations of ATZ in the sample were determined by Agilent 1290 Ultra-High Performance Liquid Chromatography (UPLC) with an Agela Venusil XPS C18 (L) column (250 mm × 4.6 mm, 5 μm). The mobile phases consisted of H_2O and ACN (30/70, v/v) at a flow rate of 0.4 mL/min. The detection wavelength was 225 nm. The injection volume was 10 μL. The column temperature was maintained at 35 °C. The total running time was 8 min.

2.5. Data analysis

The adsorption capacity of ATZ was calculated by the mass balance method according to the initial and final concentrations of ATZ in the solution and the dosage of the BC. The removal efficiency (η) of ATZ by the BC is calculated by Eq. (1):

$$\eta(\%) = \left(\frac{C_0 - C_t}{C_0}\right) \times 100 \quad (1)$$

Where C_0 is the initial concentration of ATZ (mg L^{-1}), and C_t is the concentration of ATZ (mg/L) at regular sampling. The adsorption capacity of the BC to ATZ is calculated as the following Eq. (2):

$$q_t = \frac{C_0 - C_e V}{m} \quad (2)$$

Among them, q_t represents the adsorption amount of ATZ per unit mass of BC at time t (mg/g), V represents the volume of the solution (L), C_e represents the concentration of ATZ in the aqueous phase at equilibrium (mg/L), and m is the mass of the BC (g).

Adsorption kinetics of ATZ can be fitted by First-order, Second-order, and Elovich models in Eq. (3–5) (Wang et al., 2022; Cao et al., 2024):

$$\text{First} - \text{order}: \ q_t = q_e\left(1 - e^{-k_1 t}\right) \quad (3)$$

$$\text{Second} - \text{order}: \ q_t = \frac{Q_e^2 k_2 t}{1 + Q_e k_2 t} \quad (4)$$

$$\text{Elovich}: \ q_t = \frac{1}{\beta}\ln(\alpha\beta t + 1) \quad (5)$$

Among them, q_e is the adsorption capacity of unit mass of BC to ATZ (mg/g) at equilibrium, k_1 is the first-order kinetic adsorption rate constant (h^{-1}), k_2 is the second-order kinetic adsorption rate constant (g (mg $h)^{-1}$), α is the initial adsorption rate constant (mg/g), β is the desorption constant (mg/g).

Langmuir model, Freundlich model, and Dual-mode were used to fit the experimental data of ATZ adsorption isotherms in Eq. (6–8) (Wang et al., 2022; Song et al., 2024):

$$\text{Langmuir}: q_e = \frac{q_m C_e K_L}{1 + C_e K_L} \quad (6)$$

$$\text{Freundlich}: q_e = K_f C_e^n \quad (7)$$

$$\text{Dual} - \text{mode}: q_e = \frac{bqC_e}{1 + bC_e} + K_D C_e \quad (8)$$

Where K_L represents the Langmuir constant (L/mg), q_m represents the maximum adsorption capacity (mg/g), K_f represents the affinity coefficient of the Freundlich equation [(mg/g)/(mg/L) ^{n}], n represents the nonlinear index of the Freundlich equation, and the smaller the n value, the higher the nonlinearity of the adsorption isotherm, b represents the affinity constant (L/mg), K_D represents the adsorption distribution coefficient (L/mg), and q represents the maximum adsorption capacity (mg/g).

Thermodynamics parameters such as the Gibbs free energy change (△G), enthalpy change (△H), and entropy change (△S) were calculated using Eq.(9–11):

$$K = 1000 \times K_L \times M \times C \quad (9)$$

$$\triangle G = -RT \times \ln K \quad (10)$$

$$\ln K = \frac{\triangle S}{R} - \frac{\triangle H}{RT} \quad (11)$$

Among them, K is the dimensionless constant of adsorption equilibrium after conversion. M is the molecular weight of ATZ (215.68 g/mol) and C is the standard concentration unit (1 mol/L) (Mohammed et al., 2018; Gao et al., 2023).

The statistical analyses were performed using Origin Pro 2018 (OriginLab Corp., USA). All values represent mean±standard deviation (SD) of three independent replicates unless otherwise stated. Statistical significance was assessed via one-way ANOVA with Tukey's post-hoc test in SPSS 22.0 (IBM Corp., USA).

3. Results and discussion

3.1. Characterization of the prepared BC

Surface morphology of six BC was carried out by SEM in Fig. 1. Compared with the untreated BC in Fig. 1(a-c), rough surface of the acid-treated BC was weak (Fig1.(d-f)). The PBC and APBC materials had more micropores with smaller pore size distribution than the other BC materials, related to the raw mushroom substrates of *pleurotus ostreatus* mainly composed of cottonseed shell and corncob. The OBC and AOBC materials had large and uniform pores. The LBC and ALBC material had partially regular pores, related to the raw mushroom substrates of *lentinula edodes* mainly composed of sawdust. As detailed in *Table S1*, the raw mushroom substrates of *pleurotus ostreatus, oudemansiella apalosarca*, and *lentinula edodes* were mainly composed of different percentages of cottonseed shell, corncob, bran, and sawdust with different proportions, which is the key to the difference in morphology. Microstructural features of the BC were related to the different ingredients of raw mushroom substrates (Han et al., 2023; Li et al., 2023).

Physical and chemical characteristics of the prepared BC materials were listed in Table 1. The content of C followed the rules of LBC> OBC>PBC and ALBC> AOBC>APBC, suggesting the SMS of *lentinula edodes* had high C content. Besides, the contents of C, H, and N increased, and the contents of O decreased in acid-treated BC. H/C atomic ratio serves a quantitative proxy for aromatic condensation degree in BC matrices, with lower values indicating advanced carbonization through dehydrogenation and polycyclic aromatic hydrocarbon formation during pyrolysis (Chen et al., 2008). Results indicated that the acid treatment had little influence on aromaticity and carbonization of the BC. The low H/C atomic ratios of the BC (0.23–0.34) indicated that they were highly carbonized and possessed a highly aromatic structure. O/C atomic ratio reflects polar functional group abundance and surface charge distribution, governing hydrophilicity via hydrogen bonding capacity through carboxyl/phenolic -OH groups, electron-donor characteristics affecting π-π EDA interactions, and hydration shell formation energy (Chun et al., 2004). The acid-treated BC had a lower O/C atomic ratio (0.14–0.20) than the untreated BC (0.22–0.51). The diminished O/C atomic ratio can be attributed to the effective removal of oxygenated compounds (e.g., $CaCO_3$) via acid treatment, as confirmed by the element analysis showing a reduction in oxygen content. It suggested that the acid-treated BC had low hydrophilicity, higher thermal stability, and stronger adsorption capacity. Among the six prepared BC, the AOBC had the lowest hydrophilicity and the PBC had the highest hydrophilicity. $(O + N)/C$ atomic ratio is an important parameter in the chemical properties of BC, which represents the degree of oxidation and functional group composition of BC (Zhang et al., 2011; Ahmad et al., 2012). It was found that the index of oxidation and oxygen-containing functional groups such as hydroxyl and carboxyl groups reduced in the acid-treated BC. Results suggested that the PBC had the strongest oxidation and oxygen-containing functional groups. The ash contents in the acid-treated BC decreased from 31.49–63.68 % to 10.72–45.00 %, as detailed in Table 1. The untreated BC had a high ash content, and it was related to the SMSs containing about 1 % calcium carbonate. The fact shows that acid treatment also had a significant influence on ash contents except for the bulk chemical composition.

The N_2 adsorption/desorption isotherms for the BC materials are shown in Fig. 2. The surface area, pore volume, and average pore diameter of the BC are detailed in Table 1. The surface area is followed by the rules of LBC>PBC>OBC and APBC>ALBC>AOBC. The surface area of the acid-treated BC was 1.38–5.50 times higher than that of the untreated BC. The pore volume followed by the rules of PBC>OBC>LBC and ALBC>AOBC>APBC. The pore volume of the acid-treated BC

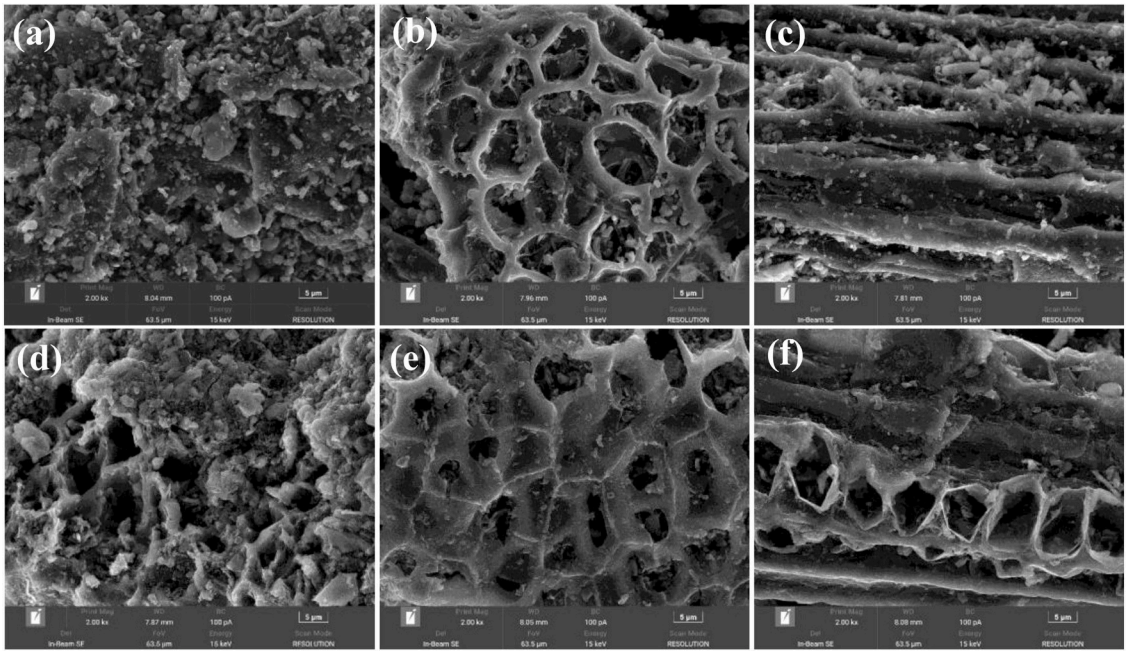

Fig. 1. SEM images of (a) PBC, (b) OBC, (c) LBC, (d) APBC, (e) AOBC, and (f) ALBC.

Table 1
Physical and chemical characteristics of the prepared BC materials.

BC	Elemental composition (%)				atomic ratio			Ash (%)	SA[a] (m^2/g)	PV[b] (cm^3/g)	PD[c] (nm)
	C	H	O	N	H/C	O/C	$(O+N)/C$				
PBC	23.94	0.67	16.31	0.61	0.34	0.51	0.53	63.68	25.29	0.068	12.03
OBC	53.43	1.07	15.55	2.63	0.24	0.22	0.26	31.49	6.72	0.042	25.17
LBC	54.99	1.13	18.89	1.85	0.25	0.26	0.29	31.49	33.97	0.037	5.57
APBC	41.74	1.10	10.98	1.11	0.32	0.20	0.22	45.00	139.15	0.084	3.65
AOBC	69.56	1.33	13.37	3.42	0.23	0.14	0.19	11.43	37.56	0.090	10.30
ALBC	70.56	1.44	14.10	2.28	0.24	0.15	0.18	10.72	46.82	0.092	8.99

[a] SA, surface area determined by the BET adsorption method.
[b] PV, pore volume.
[c] PD, average pore diameter.

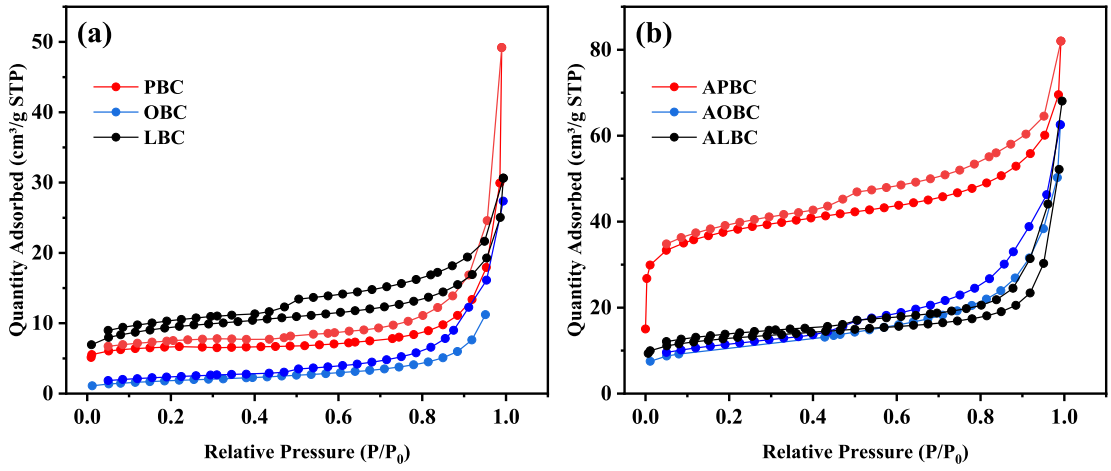

Fig. 2. N_2 adsorption-desorption isotherms of (a) BC and (b) acid-treated BC.

increased by 23 %−149 %. It indicated that the acid-treated BC trended to possess more adsorption sites and stronger pore-filling effects (Zhang et al., 2018). The average pore diameter in Fig. 3 is followed by the rules of OBC>PBC>LBC and AOBC>ALBC>APBC. The average pore diameters decreased by 69.7 % and 59.1 % in APBC and AOBC compared to PBC and OBC, respectively. However, the average pore diameters of ALBC (8.99 nm) were larger than LBC (5.57 nm). The ash existed in the pore-size tunnel of the BC, the large pore-size tunnel might collapse and form more small pores after the acid treatment, which helped to increase the specific surface area of APBC and AOBC (Hawryluk-Sidoruk et al., 2024). As described by the International Union for Pure and Applied Chemistry (IUPAC), the N_2 adsorption isotherms of the untreated BC evolved to type III, which had distinct hysteresis loop of H3 in the relative P/P_0 range of 0.45–1. After the acid treatment, the isotherms of the APBC, AOBC, and ALBC materials evolved to type II, type III, and type III, which had distinct hysteresis loops of type H4, H3, and H3 in the relative P/P_0 range of 0.45–1, respectively. Namely, that acid treatment influences adsorption behavior by altering surface chemistry and pore

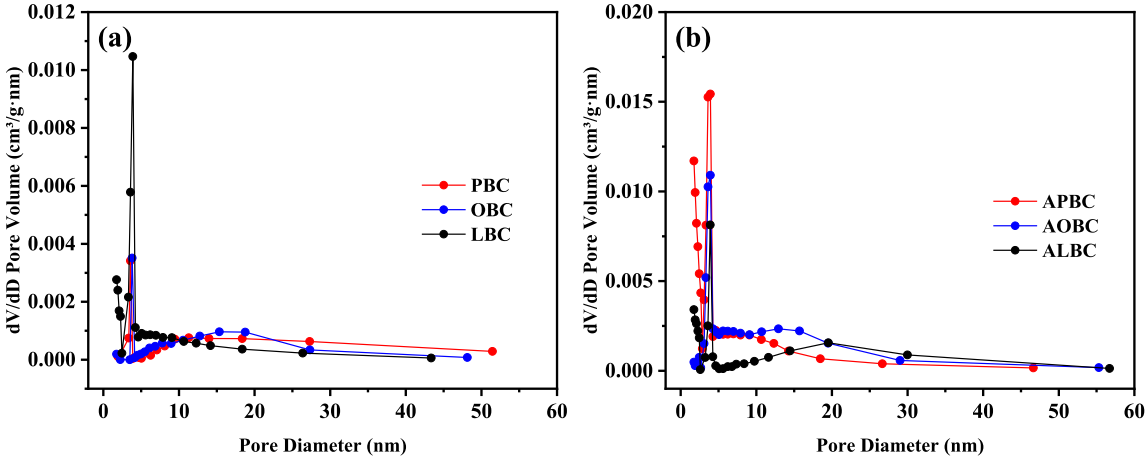

Fig. 3. Pore diameter distributions of (a) BC and (b) acid-treated BC.

structure. The specific isotherm types and hysteresis loop morphologies, however, exhibit uniqueness due to differences in raw material sources, treatment conditions, and potentially the adsorbates involved (Jing et al., 2014; Wang et al., 2022). Based on the type of distinct hysteresis loop, the APBC material might have some pores generated by layered structure, and the other BC material might have some narrow-slit holes formed by the accumulation of sheet-like particles (Jing et al., 2014) Upon further magnification at an observation ruler of 200 nm, varying degrees of wrinkles were discovered on the surface of the BC, resembling layered or flake structures.

The FTIR spectra for the six BC are shown in Fig. 4. The spectrum at ~3440 cm^{-1} is a characteristic peak for stretching vibrations of O—H in the associated state (Gao et al., 2023), ~2920 cm^{-1} were caused by C—H stretching vibrations in biopolymers (Chen et al., 2008; Zhang et al., 2011), ~1600 cm^{-1} was generated by the $C = C/C = O$ vibrations of the aromatic ring (Chen et al., 2008; Zhang et al., 2011), ~1100 cm^{-1} showed C—O stretching vibrations in structure of C—O—H (Zhang et al., 2011), ~1410 cm^{-1}, ~1060 cm^{-1}, ~870 cm^{-1}, and ~710 cm^{-1} show asymmetrical stretching vibrations, symmetric stretching vibrations, in-plane bending vibration, out-of-plane bending vibration of CO_3^{2-} (Shi et al., 2021). When heated to 900 °C, calcium carbonate will be completely decomposed into calcium oxide ($CaCO_3$) and carbon dioxide (CO_2). In the present study, BC was prepared via pyrolysis at 800 °C (< the decomposition threshold of $CaCO_3$), leading us to hypothesize that $CaCO_3$ presented within the BC matrix (Galan et al., 2013). First, acid treatment induced a noticeable reduction in the types of functional groups present in BC. For instance, characteristic peaks of carbonate (CO_3^{2-}) in FTIR spectra were significantly weakened in acid-treated BC (APBC and ALBC) compared to the pristine BC (PBC and LBC). Second, surface elemental analysis (Figure S1) directly quantified the loss of calcium (Ca) during acid treatment: the Ca content on the BC surface decreased drastically from 33.90 % (PBC) to 3.45 % (APBC). Since Ca in the SMSs is primarily bound to $CaCO_3$, this substantial reduction in surface Ca content confirms that acid treatment effectively dissolved and removed $CaCO_3$ from the BC structure. Collectively, these results demonstrate that the 800 °C pyrolysis temperature preserved $CaCO_3$ in the BC, and subsequent acid treatment selectively eliminated this carbonate component, altering both the surface chemistry and elemental composition of the biochar.

The full XPS spectra representing the chemical composition are shown in Fig. 5 (i.e., PBC and APBC) and *Figure S2-S3* (i.e., OBC and AOBC, LBC and ALBC). The peaks at 284.63~285.05 eV and 531.91~532.76 eV were attributed to the elements of C and O on the surface, respectively (Song et al., 2024). The C 1 s spectra could be deconvoluted into the peaks of C—C/C—H (284.73~284.80 eV), C—O (285.25~285.65 eV), $C = O$ (286.17~286.86 eV), and O—$C = O$ (287.83~290.27 eV) (Lou et al., 2022; Cui et al., 2024). The O 1 s spectra could be deconvoluted into the peaks $C = O$ (531.05~531.46 eV), -OH (531.96~532.86 eV), and C—O (533.01~533.74 eV) (Li et al., 2022; Peng et al., 2023). The chemical composition percentage of the BC varies depending on the type of BC. For example, for C 1 s, the C—C/C—H ratios were 25.76 %–41.88 % and 46.18 %–62.33 % in the BC and acid-treated BC, respectively. For C 1 s, the C—C/C—H ratios of the BC increased from 25.76 %–41.88 % to 46.18 %–62.33 %, the C—O ratios decreased from 24.61 %–56.44 % to 19.21–25.30 %, after the acid treatment, indicating the acid-treated BC owned strong aromatic and hydrophobicity. For O 1 s, the -OH ratios of the BC increased from 26.80 %–34.42 % to 29.95 %–59.11 % after the acid treatment, indicating the acid-treated BC might have hydrogen bond involvement. In agreement with these findings, previous research has demonstrated that the BC were characterized as carbon-rich substances that contain many functional groups and acid treatment significantly affected the chemical composition of the BC (Wang et al., 2020).

3.2. *Effects of SMS type and acid treatment on removal efficiency of ATZ*

Container adsorption was quantified by parallel blank tests (no adsorbent), showing no significant degradation at each time point (RSD <5 %) and negligible solute loss (<2 %). As demonstrated in Fig. 6, the BC prepared using the SMS of *pleurotus ostreatus* was more effective for ATZ adsorption than other two BC driven from *oudemansiella apalosarca* and *lentinula edodes*. The acid-treated BC exhibited remarkable enhancement in ATZ removal efficiency: from 17.4 % (PBC) to 98.2 % (APBC), 10.9 % (OBC) to 38.4 % (AOBC), and 7.6 % (LBC) to 27.1 % (ALBC), indicating the acid-treated BC could promote the removal efficiency of ATZ by 3.5–5.6 times. The removal performance hierarchy (PBC > OBC > LBC and APBC > AOBC > ALBC) can be comprehensively explained through the following fundamental characteristics. Acid treatment of the BC in the present study enlarged surface area and pore volume of 1.38–5.59 and 1.23–2.49 times in Table 1, respectively. The large surface area and pore volume in the acid-treated BC could provide more adsorption points for ATZ (Tan et al., 2016). APBC's superior performance (98.2 % removal) directly correlates with its developed pore structure, exhibiting highest surface area (139.15 m^2/g vs 6.72–46.82 m^2/g for others), optimal pore volume (0.092 cm^3/g) with average pore-size of 3.65 nm (higher than the diameter of ATZ molecule (~0.7 nm), and PBC's inherent microporous framework facilitated acid activation, creating additional adsorption channels. The lower H/C and

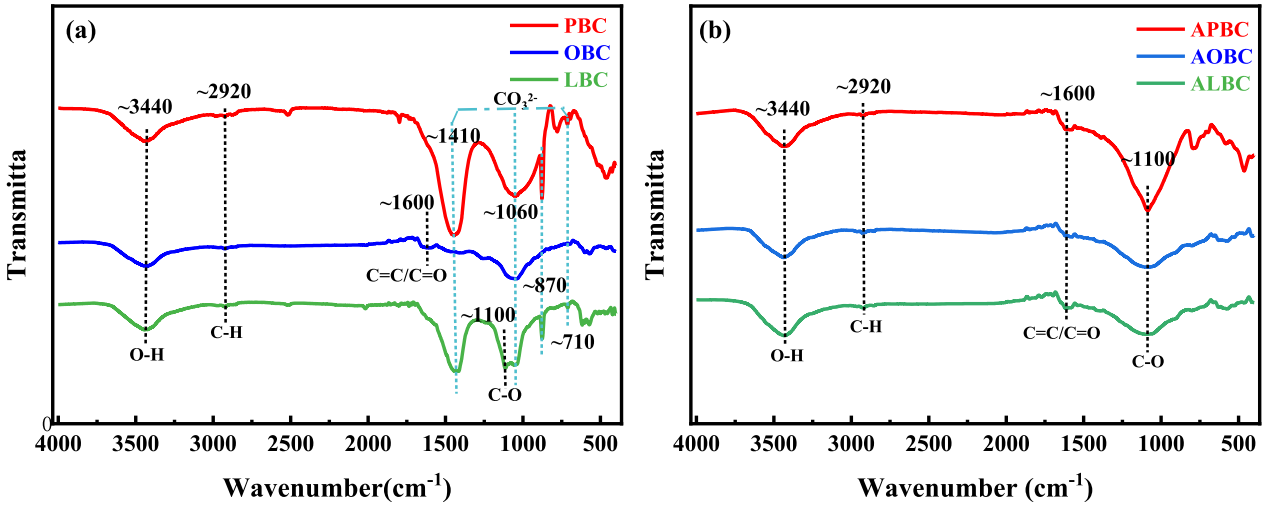

Fig. 4. FTIR spectra of (a) PBC, OBC and LBC, and (b) APBC, AOBC, and ALBC.

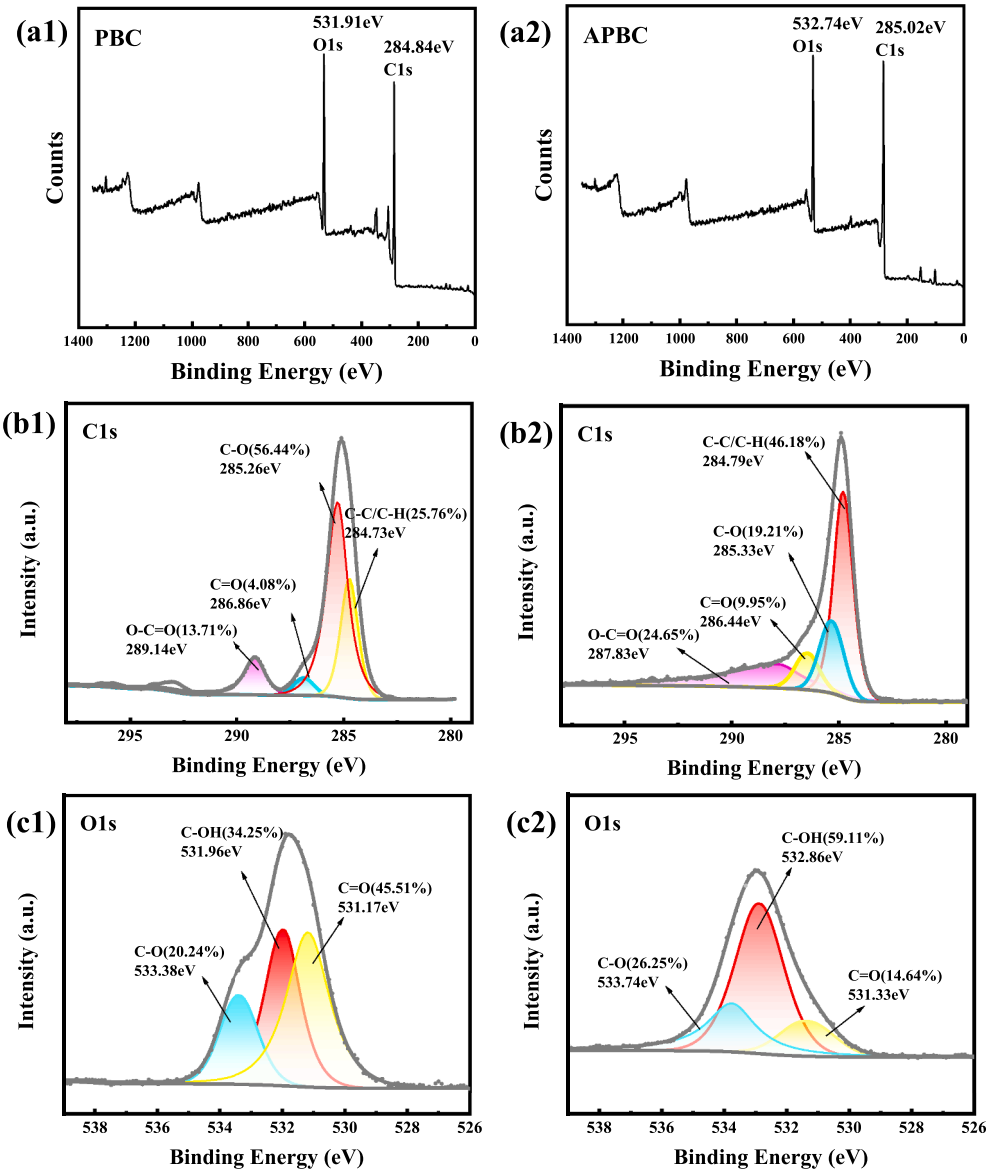

Fig. 5. XPS spectra for (a) wide survey scan, (b) O 1 s, and (c) C 1 s) of the (1) PBC and (2) APBC.

O/C atomic ratios of the BC after acid treatment BC indicated that they were highly carbonized, possessed a highly aromatic structure, and low hydrophilicity. This might help to absorb small organic pesticide molecules. XPS analysis revealed the C—C/C—H atomic ratios of the BC increased from 25.76 %–41.88 % to 46.18 %–62.33 % after the acid treatment in Fig. 4 and *Figure S2-S3*, indicating enhanced aromaticity and graphitization, and improved hydrophobic character for ATZ partitioning. The C—O atomic ratios decreased from 24.61 %–56.44 % to 19.21–25.30 % after the acid treatment, indicating selective removal of polar oxygenated groups during acid washing and development of more hydrophobic surfaces. And the -OH ratios of the BC increased from 26.80 %–34.42 % to 29.95 %–59.11 % after the acid treatment, indicating formation of new phenolic hydroxyl groups and potential for hydrogen bonding with ATZ's amine groups. FTIR analysis revealed the presence of carboxyl groups after acid treatment in Fig. 3, indicating additional sites for electrostatic interactions and enhanced capacity of cation exchange. Cooperative chemical transformations induced by acid treatment enhance ATZ adsorption on BC, thereby explaining the superior performance of the acid-treated biochar APBC. This conclusion aligns with the SHAP analysis of Chen et al. (2024), which identified biochar chemical composition (e.g., C %, N %) as the most influential factor for adsorption, ahead of other conditions.

The adsorption kinetics of ATZ on the six BC are shown in Fig. 7. The PBC and APBC showed better adsorption efficiency among the untreated and acid-treated BC. The adsorption of ATZ on the APBC, AOBC, and ALBC increased rapidly from 0 to 4.67, 1.75, and 1.37 mg/g within the first half hour, which were 13.12, 11.94, and 7.27 times of that on the PBC, OBC, and LBC, respectively. The adsorption kinetics of ATZ on the BC reached equilibrium within 24 h. Results showed that three adsorption kinetics fitted the ATZ adsorption data well, and corresponding fitting parameters and coefficients of determination are detailed in Table 2. Compared with First-order (R^2, 0.952–0.998) and Second-order (R^2, 0.967–0.998) models, Elvoich model (R^2, 0.974–0.999) had better fitting performance. The high Elovich α values of ATZ on acid treatment BC reflected abundant high-energy adsorption sites and favorable electrostatic potential gradients. The β parameter

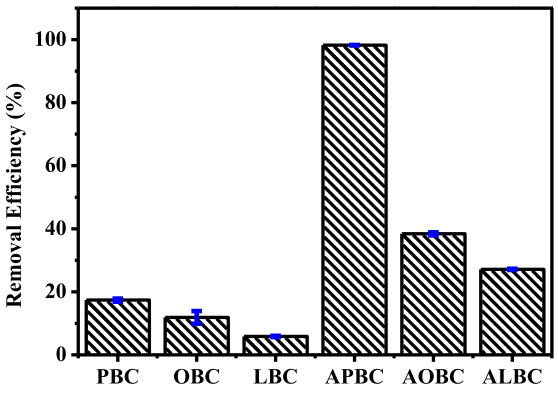

Fig. 6. Effect of the different BC on the ATZ removal efficiency. (Experimental conditions: $[ATZ]_0 = 10$ mg/L, m(BC) =25 mg, $V = 25$ mL, pH = 5.9, $t = 24$ h, $T = 25$ °C)3.3 Adsorption Kinetics.

range (7.12±0.62 - 79.25±85.49 g/mg) indicated activation energy requirements and presence of diffusion limitations. Results showed an adsorption behavior of ATZ on a heterogeneous BC surface, which was controlled by a multi-mechanism process (Wang et al., 2022; Cao et al., 2024). The kinetic data combined with our characterization results might have the following operative mechanisms. Firstly, initial rapid phase (0–2 h) might be controlled by physical adsorption (π-π EDA interactions) and pore filling in BC's mesoporous structure (2–50 nm). Secondly, intermediate phase (2–8 h) might be governed by hydrogen bonding dominating (increased -OH groups) and intraparticle diffusion. Thirdly, the final equilibrium phase (8–24 h) might be limited by chemisorption prevails (Elovich behavior) and involve covalent bonding with carboxyl groups.

3.4. Adsorption isotherms

The adsorption isotherms of ATZ on the BC are shown in Fig. 8. Parameters of three isotherm models are listed in Table 3. Among them, the Dual-mode had a better fitting performance for the ATZ on the BC with R^2 ranging from 0.981 to 0.999. It indicated that the adsorption of ATZ was not a single-layer reversible adsorption, but rather partition and multi-layer adsorption (Tan et al., 2016). The Freundlich model also show a good fitting the ATZ on the BC (R^2 >0.97). The corresponding K_f values for the APBC were 8.55±0.62 (mg/g)/(mg/L)^n, which were 8.07, 7.25, and 9.19 times of that for the PBC, AOBC, and ALBC, respectively. This significant enhancement directly demonstrates that acid treatment drastically improved the adsorption affinity of biochar for the target contaminant. The nonlinear coefficient n in range of 0.25±0.048 - 0.52 ±0.015 in the Freundlich model reflected the heterogeneity of adsorption sites and the distribution of adsorption energies. A smaller n value indicates greater heterogeneity and low-energy adsorption sites, with a higher proportion of high-energy sites. The ATZ adsorption capacities for APBC, AOBC and ALBC were 13.54, 4.20 and 4.03 mg/g, respectively. The enhancement in adsorption performance for BC was achieved by the acid treatment, which was consistent with previous studies (Zhang et al., 2018; Wang et al., 2020). The max adsorption capacities of APBC for ATZ were also higher than the reported BC (0.6–0.8 mg/g), acid-treated BC (1.0–1.2 mg/g), and montmorillonite-BC (2.5–3.0 mg/g) driven from peanut shell (Wang et al. 2020; Wang et al., 2022), washed peanut shells BC (2.1 mg/g) (Wang et al., 2025), citric acid modified biogas-residue BC (5.9 mg/g) (Cao et al., 2024), respectively. This indicates that the SMS driven BC is also one excellent biomass for the pesticide adsorption..

3.5. Adsorption mechanisms

Organic carbon within the BC serves as the primary adsorptive domain for the ATZ), playing a pivotal role in governing the adsorption process. To quantify the OC-dependent adsorption behavior, concentration-normalized organic carbon partition coefficients (K_{OC}) were calculated across five ATZ equilibrium concentrations ($C_e = 0.01$, 0.1, 1, 10, and 25 mg/L) (*Table S2*). The resulting adsorption isotherms exhibited characteristic layer saturation behavior, where incremental ATZ loading progressively occupied available binding sites until attaining equilibrium capacity. The concentration-dependent decline in $\log K_{OC}$ values across tested ATZ levels quantitatively reflected site energy heterogeneity, as evidenced by Freundlich nonlinearity coefficients ($n < 1$). This energetic dispersion might originate from high-affinity sites (micropore filling and π-π EDA interactions), intermediate sites (Partitioning into amorphous carbon phases and hydrogen bonding with phenolic -OH groups), and low-energy sites (Surface precipitation and physisorption on mesopores) (Wang et al., 2020; Liu et al., 2023). Notably, the acid-treated BC (e.g., APBC) exhibited favorable properties for enhancing OC-mediated adsorption, and it had low ash content (minimizing interference from inorganic matrices), high carbon content (enriching OC functional groups), and strong hydrophobicity (promoting ATZ partitioning, given ATZ's hydrophobic nature). These characteristics collectively amplified the contribution of OC-dominated sites over ash-associated sites. The significantly enhanced $\log K_{OC}$ values of APBC (compared to non-treated BC) thus directly indicates that ATZ exhibited greater adsorption affinity for the OC-enriched functional sites in APBC than for the limited ash-based adsorption sites, underscoring the critical role of OC in driving efficient ATZ removal.

Regression modeling revealed significant structure-activity relationships between BC characteristics and ATZ partitioning behavior. In Fig. 9(a), the inverse proportionality of Freundlich linearity indices with $\log K_{OC}$ values (R^2>0.636, $P < 0.05$), indicating that BC with higher 1/n exhibits higher $\log K_{OC}$ with stonger ATZ affinity. Notably, the acid-treated BC exhibited higher ATZ affinity coefficients and reduced isotherm nonlinearity, and it was consistent with the literature study (Wang et al., 2020). It aligns with our prior findings (Section 3.2) that acid treatment enriches high-affinity functional groups and reduces inorganic ash, thereby homogenizing the adsorption site distribution and enhancing binding uniformity and directly validated by the improved linearity of APBC's Freundlich isotherm. At high ATZ equilibrium concentrations (Ce >10 mg/L), Fig. 9(b) revealed a positive correlation between the $\log K_{OC}$ values and H/C atomic ratios when C_e was higher than 10 mg/L (R^2>0.585, $P < 0.05$). Since H/C ratio is inversely proportional to aromatic carbon content (higher aromaticity corresponds to lower H/C), this positive relationship indirectly reflects the dominance of aromatic domains in driving ATZ adsorption at high concentrations (Chen et al., 2008). It aligns with the earlier characterization (Table 1) that APBC exhibits high carbon content and extensive aromaticity due to pyrolysis, which provides abundant π−conjugated sites for ATZ's electron-deficient triazine ring to engage in π-π EDA interactions (Ji et al., 2011; Lattao et al., 2014). For low ATZ concentrations (Ce <1 mg/L), Fig. 9(c) showed a positive correlation between the $\log K_{OC}$ values and surface area (R^2>0.585, $P < 0.05$). It suggested that at dilute conditions, where ATZ molecules are sparsely distributed, pore filling becomes the rate-limiting step for adsorption. It resonates with the prior analysis of APBC's pore structure (Section 3.1), where acid treatment removes inorganic ash and expands porous volumes, thereby increasing the availability of pore spaces for ATZ partitioning. Collectively, these regression results bridge our earlier characterization with quantitative adsorption behavior. They confirm that acid treatment optimizes BC's adsorption site distribution via reducing nonlinearity, aromatic domains dominate high-concentration adsorption via π-π EDA interactions, and pore filling drives low-concentration adsorption.

In addition, there are no obvious correlations between the $\log K_{OC}$ values and O/C atomic ratios and $(O + N)$/C atomic ratios, as presented

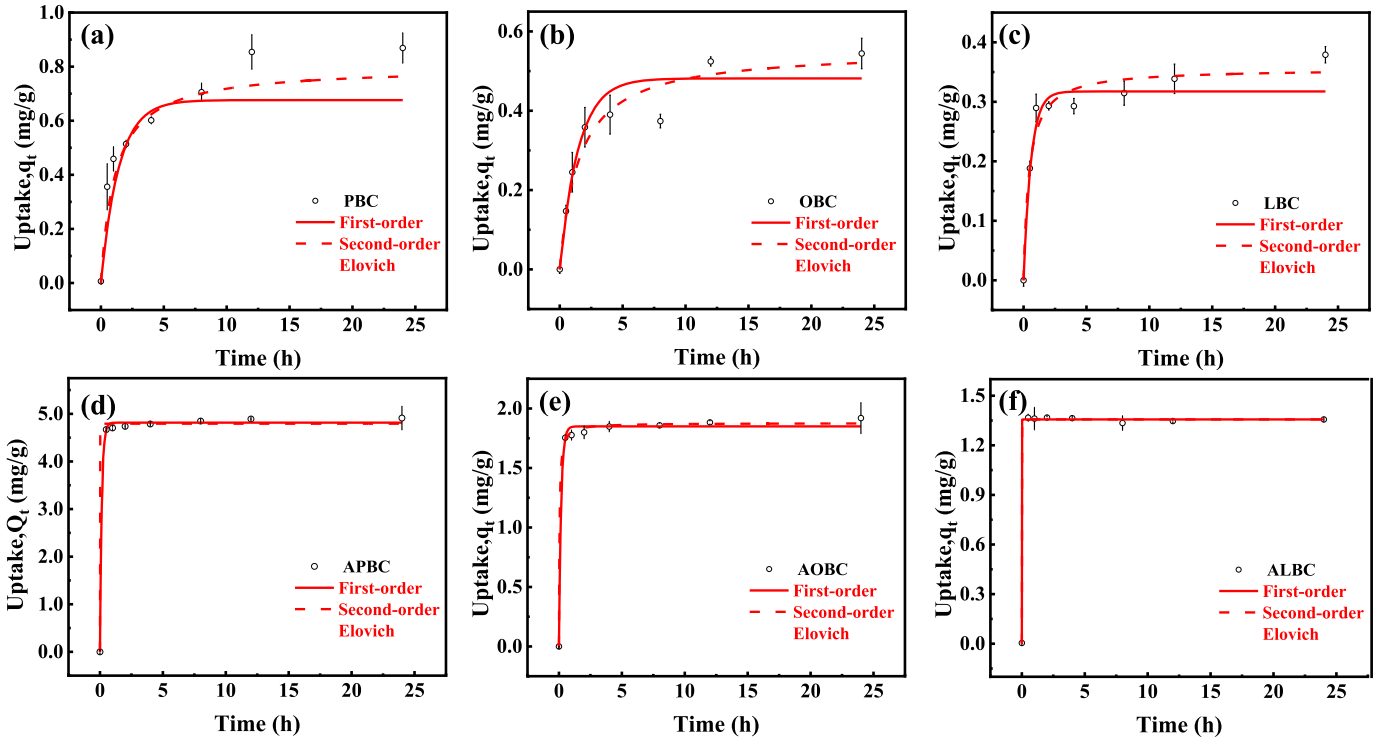

Fig. 7. Adsorption kinetics of ATZ on the (a) PBC, (b) OBC, (c) LBC, (d) APBC, (e) AOBC and (f) ALBC. (Experimental conditions: $[ATZ]_0 = 10$ mg/L, m(BC) = 25 mg, $V = 25$ mL, pH = 5.9, $t = 24$ h, $T = 25$ °C).

Table 2
Fitting parameters of adsorption kinetics of ATZ on the BC.

BC	First-order			Second-order			Elovich		
	q_e(mg/g)	K_1(1/h)	R^2	q_e(mg/g)	K_2(g/(mg·h))	R^2	α(mg/g)	β(g/mg)	R^2
PBC	0.68±0.047	0.71±0.17	0.977	0.80±0.052	1.106±0.34	0.991	2.66±0.75	7.12±0.62	0.998
OBC	0.49±0.029	0.67±0.23	0.952	0.55±0.041	1.17±0.52	0.967	0.57±0.25	8.15±1.31	0.977
LBC	0.32±0.014	1.70±0.40	0.956	0.36±0.014	6.46±1.66	0.980	14.56±14.89	23.51±4.06	0.974
APBC	4.82±0.031	6.921±0.08	0.998	4.79±0.11	6.44±0.44	0.996	2.11±8.01	14.92±0.80	0.999
AOBC	1.85±0.019	5.78±0.99	0.994	1.88±0.015	12.49±3.07	0.998	5.83±12.64	23.48±1.21	0.999
ALBC	1.36±0.041	275.10±0.01	0.993	1.36±0.041	6.26±0.001	0.993	3.28±328.72	79.25±85.49	0.993

in *Figure S4*. However, a notable negative correlation was observed between the logK_{OC} values and $(O + N)/C$ atomic ratios during the ATZ adsorption onto peanut shell BC (Wang et al., 2020). This pattern aligns with similar observations in neonicotinoids adsorption on the BC driven from maize straw and pig manure, where $(O + N)/C$ ratios also exhibited inverse relationships with log*KOC* (Zhang et al., 2018). It suggested that these relationships might be more easily discovered on BC using homogeneous biomass materials with different temperature pyrolysis (Zhang et al., 2018). In our study, the hydrophobicity of the deashed BC increased with the decrease of O/C atomic ratios from 0.26–0.53 to 0.18–0.22. The acid-treated BC could significantly promote the removal efficiency of ATZ by 3.5–5.6 times that of the untreated BC, indicating that hydrophobicity was also one key factor determining the adsorption of the ATZ on the BC driven from different SMSs. The K_{OC} values decreased with the increase of ATZ concentration, also indicating the hydrophobicity played a critical role at high solute adsorption sites. As referred, the -NH and -H on the ATZ can form hydrogen bonds with -OH and $C = O$ functional groups on the BC surface (Gao et al., 2023). The decrease of O content after the acid treatment (Table 1) significantly affected the richness of functional groups (Fig. 4) and composition of the BC surface (Fig. 5 and *Figure S2-S3*). It was inferred that the acid BC had a stronger hydrophobicity and weaker hydrogen bond formation during the ATZ adsorption compared with the untreated BC.

Overall, the ATZ adsorption mainly included pore filling, hydrophobic partition, π-π EDA interactions, and hydrogen bonding mechanisms (Gao et al., 2023; Wang et al., 2022). In addition, a graphical adsorption mechanisms assignment of ATZ on PBC, OBC, LBC, APBC, AOBC, and ALBC was investigated refer to the reported literatures (Li et al., 2022; Wang et al., 2024). Quantification adsorption mechanisms assignment was achieved through competitive adsorption (*Text S1*). As shown in Fig. 10, the PBC and OBC exhibited dominant hydrophobic partitioning (45.2–47.2 %) and π-π EDA interactions (47.3–49.8 %) evidenced by their high aromaticity. In contrast, LBC's adsorption relied more on hydrophobic effects (31.2 %) and hydrogen bonding (35.4 %), supported by its elevated oxygen content and distinct phenolic -OH FTIR peaks. Acid treatment induced a consistent 30–40 % reduction in hydrophobicity contribution across all the BC, with emerging dominance of pore filling (36.3–42.4 %), preserved π-π interactions (20.4–31.1 %), and enhanced hydrogen bonding (27.6–35.0 %) from newly formed -COOH/-OH groups. The findings demonstrate that BC adsorption mechanisms are tunable by both intrinsic properties and extrinsic modifications. For PBC/OBC, the lignin-derived aromaticity makes them inherently suited for hydrophobic partitioning and π-π EDA-driven adsorption, while LBC's structure favors hydrophobic effects and hydrogen bonding. Acid treatment, by modifying surface chemistry and pore structure, redirects the dominant mechanism from hydrophobic partitioning to a synergistic combination of pore filling, preserved π-π EDA interactions, and enhanced hydrogen bonding.

3.6. Effects of temperature, pH, inorganic salt, and HA

Experiment data in Fig. 8 demonstrated that APBC exhibited superior ATZ adsorption capacity relative to other tested BC. To establish fundamental relationships between environmental parameters (temperature, pH) and adsorption behavior, APBC was selected as the representative material given its optimal performance. When the adsorption temperature was elevated to 35 °C and 45 °C (Fig. 11), the adsorption kinetics of ATZ on the APBC exhibited stronger correspondence with the Elovich model, while the adsorption isotherms were better described by the Dual-mode model. These model selections are supported by quantitative fitting parameters in *Tables S3 and S4*. Results indicated that the temperature didn't affect the optimal usage model of the ATZ adsorption onto the APBC.

The adsorption thermodynamic parameters of ATZ on the APBC (Table 4) provide critical insights into the temperature dependence of adsorption efficiency, directly linking macroscopic performance (e.g., q_e, K_D) to microscopic molecular interactions. The negative Gibbs free energy change ΔG (<0) confirms that ATZ adsorption onto APBC is a spontaneous and thermodynamically favorable process at all tested temperatures (25–45 °C). It means no external energy input is required to drive the adsorption, making APBC a passive yet effective adsorbent for ATZ remediation. The positive enthalpy change ΔH (41.16 kJ/mol) indicates that ATZ adsorption on APBC is endothermic, requiring thermal energy to overcome repulsive forces between ATZ molecules and the APBC surface. This can explain that q_e and K_D increased with temperature. The positive entropy change △S (250.90 J/(mol·K)) illustrated that the change of the freedom degree of the ATZ molecules and the increase of disorder on the solid-liquid interface and during adsorption (Mohammed et al., 2018; Gao et al., 2023). The obtained values are physically reasonable. A ΔH value of 41.16 kJ/mol is below 80 kJ/mol, which is consistent with a physisorption-dominated process. The significant positive ΔS is a common and logical feature in adsorption from aqueous solution, primarily attributed to the release of structured water molecules upon adsorption, as previously described. The consistent decrease in ΔG with increasing temperature is also thermodynamically sound for an endothermic process. In summary, the process is spontaneous (ΔG < 0), endothermic (ΔH > 0), and entropy-driven (ΔS > 0), pointing to a physisorption-mediated mechanism facilitated by the dehydration of hydrophobic surfaces and the resulting increase in system disorder.

As described in Fig. 12(a), the effect of initial pH values of the aqueous solution on the adsorption capacity of ATZ on the APBC was studied. With the increase of pH from 2.9 to 10.4, the adsorption of ATZ slightly decreased from 8.79 mg/g (pH=2.9) to 8.56 mg/g (pH=10.4). pH values of aqueous solution can change the ionization degree of ATZ molecules. As referred, pK_a value of ATZ is 1.7, which indicates ATZ is a weakly alkaline pesticide and mainly exists as neutral molecules, and protonates the triazine cations formation of ATZ at very low pH values (Gao et al., 2023). The zeta potential of the APBC is shown in *Figure S5*. It suggested that the positive charges on the APBC surface under strong acid conditions. Hence, it is not conducive to ATZ adsorption under neutral and alkaline conditions.

Fig. 12(b) shows the effects of NaCl, $NHCO_3$ and HA on the ATZ adsorption capacity by the APBC. In the presence of NaCl and $NaHCO_3$, the adsorption of ATZ were 8.69±0.25–8.76±0.53 mg/g and 8.76 ±0.12–8.79±0.40 mg/g, respectively. The adsorption of ATZ were 9.00 ±0.08 and 8.65±0.35 mg/g in the presence of 1 and 10 mg/L HA,

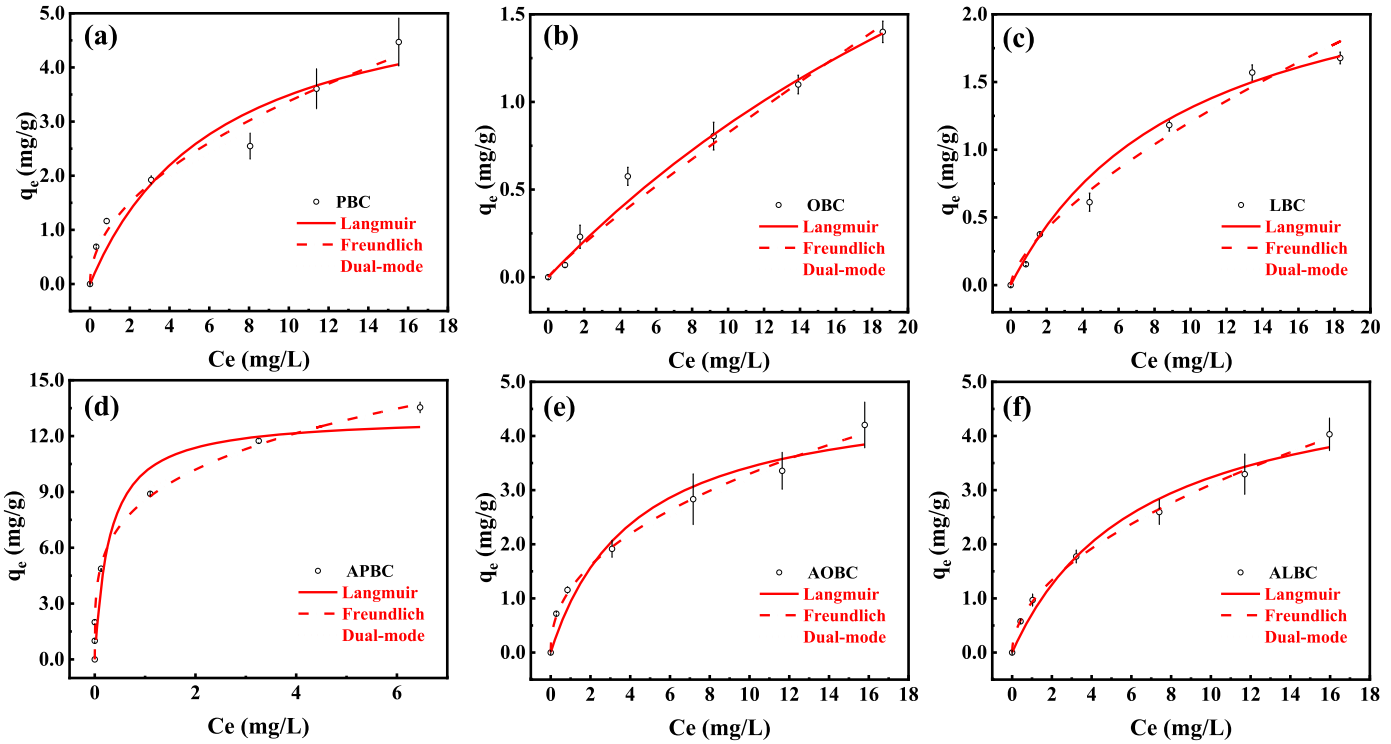

Fig. 8. Adsorption isotherms of ATZ on the (a) PBC, (b) OBC, (c) LBC, (d) APBC, (e) AOBC and (f) ALBC. (Isotherm data were fitted to Langmuir, Freundlich, and dual-mode models. Experimental conditions: $[ATZ]_0$ = 10 mg/L, m(BC) = 25 mg, V = 25 mL, pH = 5.9, t = 24 h, T = 25 °C).

Table 3
Fitting parameters of adsorption isotherms of ATZ on the BC.

BC	Langmuir			Freundlich			Dual-mode			
	q_m (mg/g)	K_L (mL/(mg))	R^2	K_f (mg/g)/(g/L)^n	n	R^2	b (L/g)	q (mg/g)	K_D (L/g)	R^2
PBC	5.76±1.52	0.15±0.1	0.878	1.06±0.15	0.50±0.06	0.973	1.23±0.27	3.95±3.31	0.21±0.022	0.988
OBC	4.54±2.36	0.024±0.016	0.981	0.10±0.022	0.90±0.080	0.980	0.024±0.018	4.50±3.59	5.62±0.03	0.981
LBC	2.61±0.30	0.10±0.015	0.977	0.26±0.017	0.66±0.041	0.966	0.10±0.015	2.61±0.30	1.57±0.01	0.981
APBC	13.06±1.25	3.37±1.80	0.858	8.55±0.62	0.25±0.048	0.965	9.42±1.88	7.97±5.65	0.69±0.37	0.955
AOBC	4.87±0.71	0.24±0.10	0.925	1.18±0.065	0.45±0.023	0.995	1.66±0.17	2.15±0.65	0.16±0.013	0.996
ALBC	5.34±0.71	0.15±0.05	0.965	0.93±0.033	0.52±0.015	0.998	1.63±0.067	1.02±0.097	0.16±0.0044	0.999

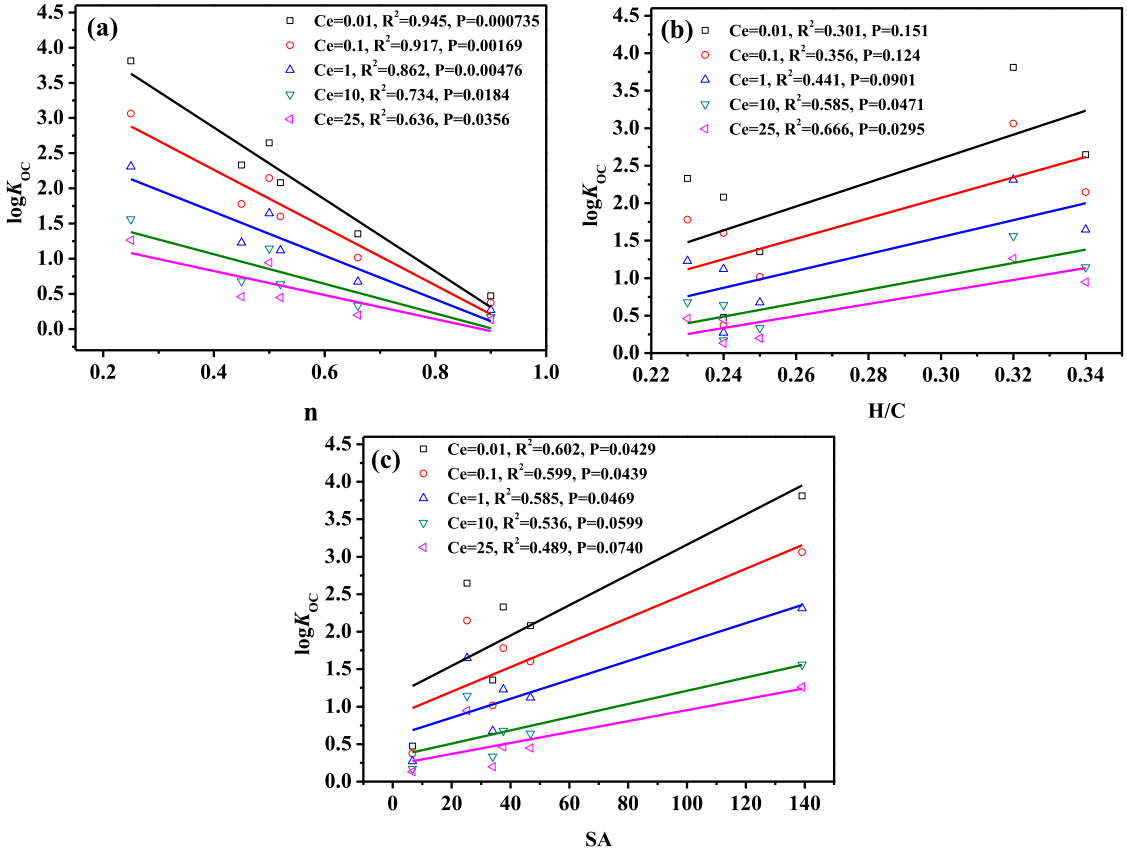

Fig. 9. Correlations of BC characteristics with the adsorption isotherm parameters of ATZ. (n, Freundlich nonlinearity coefficients; H/C, H/C atomic ratio; SA, surface area of BC).

respectively. In the present study, NaCl, $NaHCO_3$ and HA exerted no statistically significant influence on the ATZ adsorption ($P < 0.05$) under the tested experimental conditions. This discrepancy between theoretical expectations and experimental observations could be attributed to that the experimental concentration ranges of NaCl, $NaHCO_3$, and HA might have been insufficient to trigger measurable changes in BC's key properties. For instance, the ionic strength from NaCl may not have reached the threshold required to compress the electrical double layer on BC surfaces (Li et al., 2022), or the pH adjustment by $NaHCO_3$ might have been too mild to alter the dissociation state of BC's oxygen-containing functional groups (e.g., -COOH, -OH) significantly (Gao et al., 2023). Similarly, the dosage of HA might have been too low to effectively coat BC pores or compete with ATZ for adsorption sites, failing to induce observable modifications in surface polarity or hydrophobicity (Gao et al., 2023; Liu et al., 2022).

3.7. Environmental relevance and reusability of the APBC

Experiment to quantitatively evaluate the adsorption performance across different production batches was conducted. To ensure consistency within our study, a large composite batch was thoroughly mixed, dried, and homogenized before pyrolysis, minimizing intra-batch variability. Three independent batches of APBC under identical conditions. The adsorption performance of each batch was tested against 10 mg/L of ATZ. The results demonstrated excellent consistency that the removal rates were 96.5 ± 2.3 %, 98.2 ± 3.9 %, and 98.5 ± 3.5 % for the three batches, respectively. The narrow range of variation strongly indicates that the adsorption performance of the APBC is highly reproducible despite potential minor variations in the present study.

Adsorption experiments at trace concentrations of ATZ (0.0005 mg/L, 0.005 mg/L, 0.05 mg/L, and 0.5 mg/L) on the APBC were conducted. The aqueous phase ATZ concentration before and after adsorption was quantitatively analyzed using Liquid Chromatography-Mass

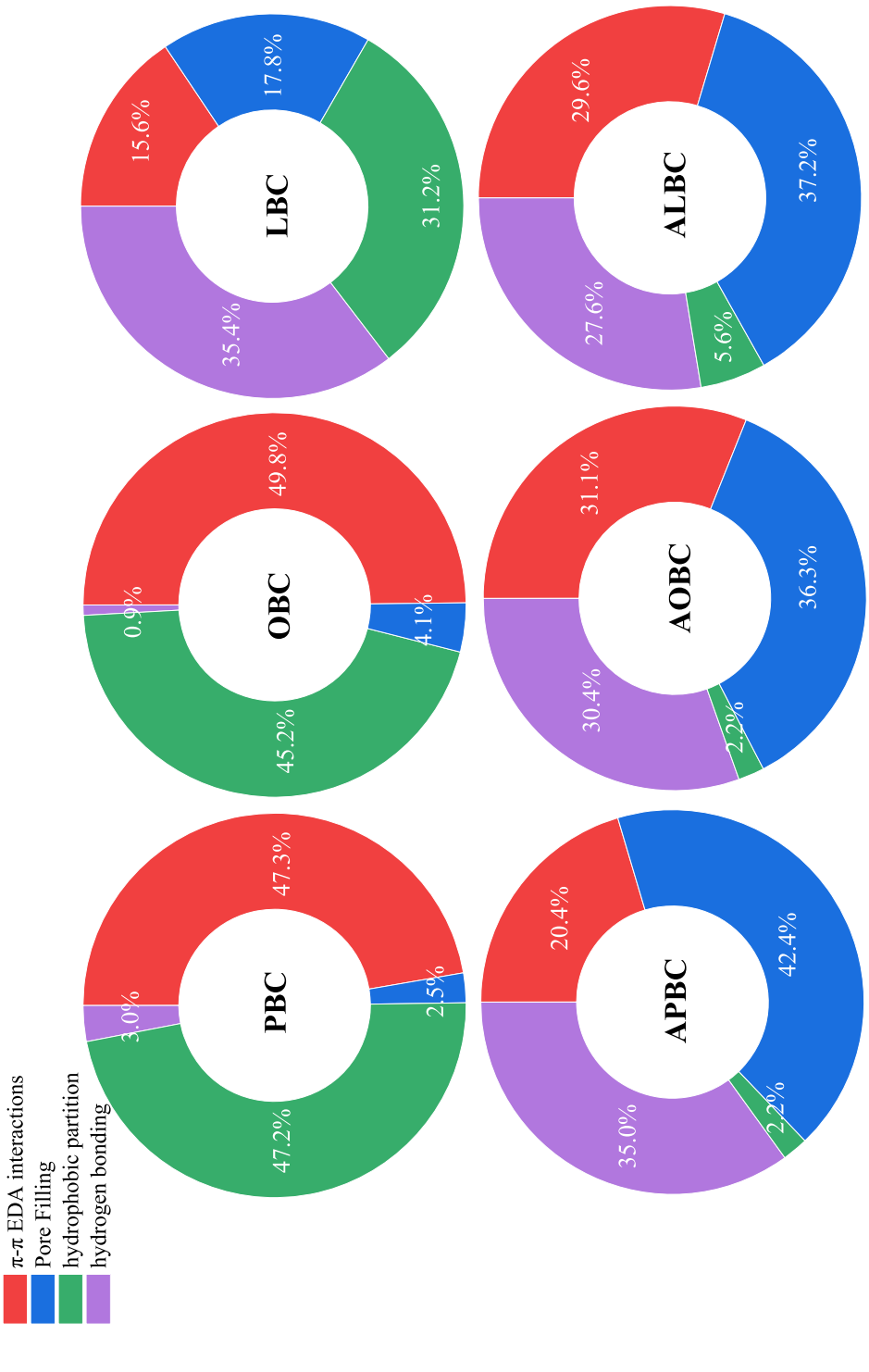

Fig. 10. Adsorption mechanisms assignment of ATZ adsorption onto the PBC, OBC, LBC, APBC, AOBC, and ALBC.

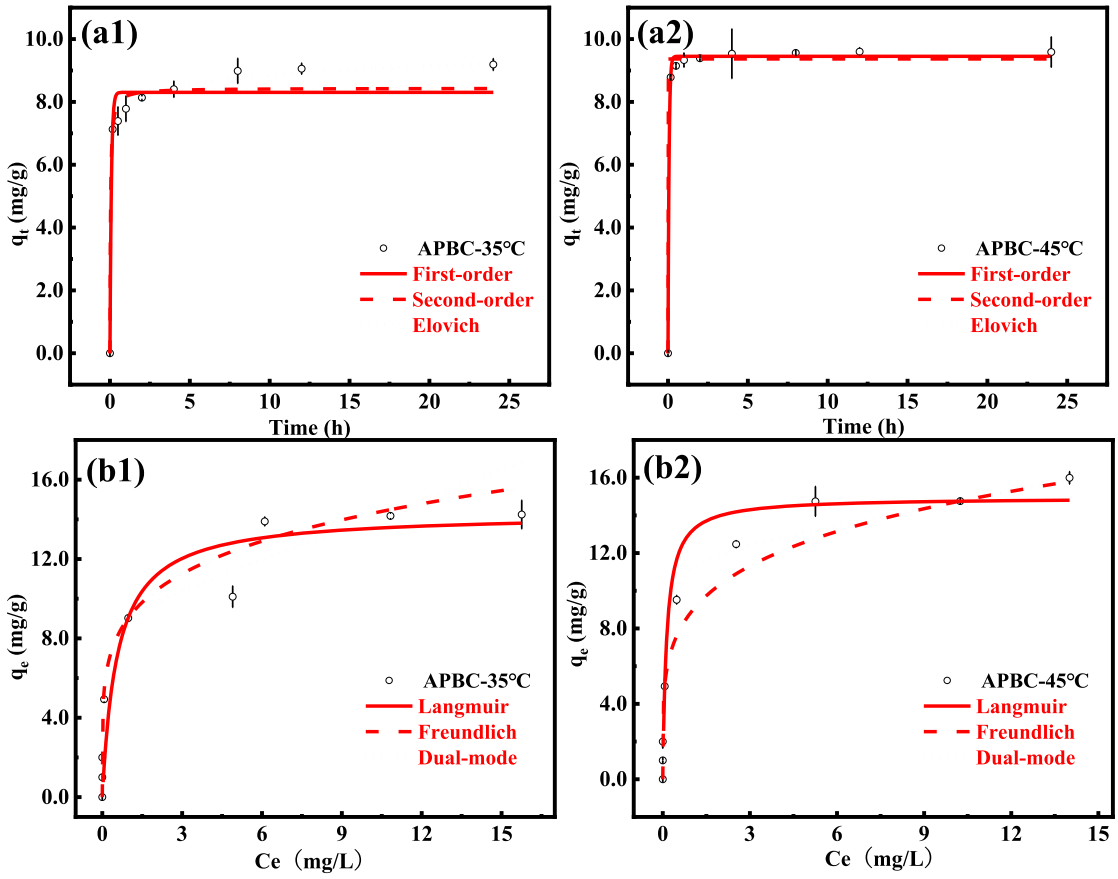

Fig. 11. (a) Adsorption kinetics and (b) isotherms of ATZ on the APBC at (1) 35 °C and (2) 45 °C. (Experimental conditions: $[ATZ]_0$ = 10 mg/L, m(BC) = 25 mg, V = 25 mL, pH = 5.9, t = 24 h).

Table 4
The adsorption thermodynamic parameters of ATZ on the APBC.

pesticide	Temperature (°C)	ΔG (kJ/mol)	ΔH (kJ/mol)	ΔS (J/(mol·K))
ATZ	25	−33.45	41.16	250.90
	35	−39.69		
	45	−41.02		

Spectrometry (LC-MS/MS) to ensure accuracy at these low levels. The removal efficiency of ATZ by APBC was consistently greater than 99 %. Achieving removal efficiency indicates the presence of a substantial number of high-energy adsorption sites on the APBC surface that exhibit a powerful attraction for ATZ. These sites likely result from the specific pore structure and surface chemistry formed by the high-temperature pyrolysis and acid modification. This strongly proves that the adsorption process is spontaneous and intensely thermodynamically driven, perfectly consistent with the negative ΔG value concluded in the earlier thermodynamic analysis. Results demonstrate that the APBC possesses an exceptionally high adsorption affinity for ATZ.

To test the intrinsic stability and capacity retention under repeated use, five consecutive adsorption cycles at 0.5 mg/L were performed using the APBC without any regeneration between cycles. This simulates a scenario of continuous exposure. The removal rates were consistently high of 99.8 % (cycles 1), 95.6 % (cycles 2), 92.6 % (cycles 3), 84.5 % (cycles 4), and 72.6 % (cycles 5), respectively. The gradual decline is due to the natural saturation of active sites, and the good removal efficiency after the fifth cycle highlights the APBC's excellent durability.

The post-adsorption characterization of the APBC provides compelling evidence for the successful uptake of ATZ (***Figure S6***). The increased surface roughness observed via SEM suggests the accumulation of ATZ molecules on the biochar's surface. More critically, EDS mapping confirmed the uniform distribution of chlorine (Cl) element, a constituent of ATZ, across the carbon matrix, which serves as direct elemental proof of ATZ adsorption. Furthermore, the notable decrease in specific surface area (81.0 m^2/g), pore volume (0.073 cm^3/g), and average pore size (3.62 nm), as determined by BET analysis, indicates that adsorption occurred not only on the external surface but also within the intricate pore network. This led to partial pore filling and blockage, a common phenomenon in adsorption processes that effectively explains the reduction in textural parameters. The combination of these findings (morphological change, elemental evidence, and pore structure alteration) forms a robust line of evidence confirming ATZ was effectively adsorbed onto and into the APBC.

Assessing the potential for secondary pollution is paramount for evaluating the environmental safety of our adsorbent. Preliminary leaching tests by agitating the APBC in neutral-pH water for 24 h were performed, followed by analysis of the supernatant. Release concentration of cation ions Na^+, K^+, Mg^{2+}, and Ca^{2+} were 0.24, 0.25, 0.49, and 0.45 mg/L (below than 0.5 mg/L). The TOC analysis revealed that the acid-treated biochar (APBC) released 3.7 mg/L of organic compounds into the aqueous phase but achieved a 37.3 mg/L reduction in the TOC of ATZ-contaminated water. This demonstrates that the environmental benefit of TOC removal far outweighs the potential risk of

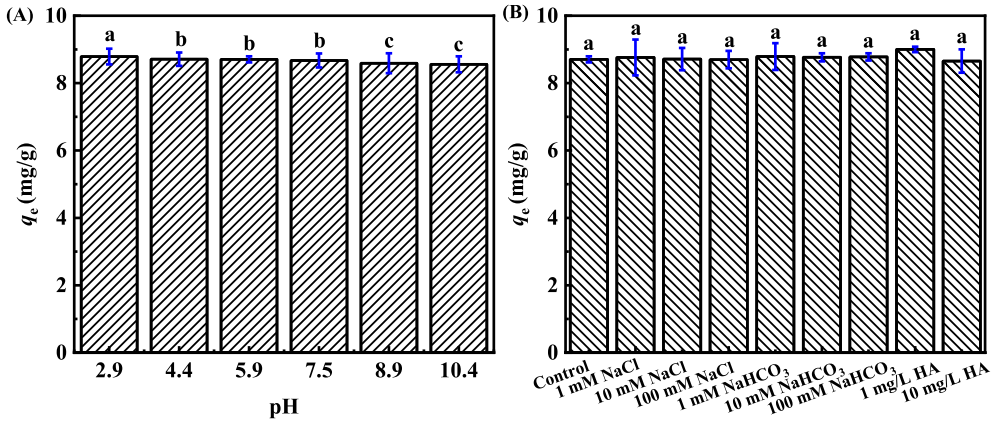

Fig. 12. Effects of (A) pH, (B) inorganic salts and HA on the ATZ adsorption on the APBC. (Except for the investigated parameter, the other reaction parameters were fixed at: $[ATZ]_0$ = 10 mg/L, m(BC) = 25 mg, V = 25 mL, pH =5.9, t = 24 h).

secondary pollution. These new findings confirm that the APBC is not only an effective adsorbent but also an environmentally safe material with low risks of secondary contamination.

Overall, the APBC material demonstrates highly stable and reproducible excellent adsorption performance across different production batches, achieving over 99 % removal efficiency for ATZ even at trace concentrations, proving its adsorption process to be spontaneous and highly efficient. After five consecutive uses, it still maintains a removal rate of 72.6 %, indicating good durability, and post-adsorption characterization directly confirms the effective adsorption of ATZ into the material's internal structure. Additionally, leaching tests show that the material exhibits high stability in water, with extremely low release concentrations of ions and organic compounds, making it an effective and environmentally safe adsorbent with minimal risk of secondary pollution.

4. Conclusions

The BC and acid-treated BC driven from three SMSs of *pleurotus ostreatus, oudemansiella apalosarca*, and *lentinula edodes* through 800 °C pyrolysis was firstly prepared in the present study. Comprehensive characterization reveals that the physicochemical properties of the BC materials are significantly influenced by both the feedstock origin and acid treatment. Elemental analysis and atomic ratios confirmed that all the BCs are highly carbonized and aromatic. Acid treatment effectively tailors the BC's adsorptive properties by enhancing surface area, porosity, and aromaticity while reducing hydrophilic ash components. FTIR and XPS analyses further indicated a reduction in oxygen-containing functional groups (e.g., carbonates, C–O) and a relative increase in aromatic C–C/C–H content in acid-treated BC. The removal efficiency of ATZ by the BC followed the rules of APBC (98.2 %) > AOBC (38.4 %) > ALBC (27.1 %) and PBC (17.4 %) > OBC (10.9 %) > LBC (7.6 %) in an aqueous solution. The SMS of *pleurotus ostreatus* is a more promising source of BC for ATZ adsorption. The acid-treated BC promoted the removal efficiency of ATZ by 3.5–5.6 times, indicating that acid treatment is an effective means of modifying SMS-BC. Kinetic and isotherm models suggested that adsorption process of ATZ on the BC was controlled by heterogeneous surface interactions and multi-mechanisms. The enhanced $\log K_{OC}$ values of acid-treated BC indicated that ATZ exhibited greater adsorption affinity for the OC-enriched functional sites. It suggested that acid treatment optimizes BC's adsorption site distribution via reducing nonlinearity, aromatic domains dominate high-concentration adsorption via π-π EDA interactions, and pore filling drives low-concentration adsorption. Furthermore, mechanistic analysis quantified four dominant adsorption pathways with distinct contribution ranges: pore filling (2.2–42.4 %), hydrophobic partitioning (2.2–47.2 %), π-π electron donor-acceptor interactions (15.6–49.8 %), and hydrogen bonding (0.9–35.0 %). Thermodynamic analysis indicated that the ATZ adsorption on the BC was spontaneous and endothermic, and the entropy was increasing in the adsorption process. High temperature and acidic conditions are conducive to ATZ adsorption. The APBC material exhibitsed excellent batch-to-batch reproducibility and maintains over 99 % ATZ removal efficiency at trace concentrations, demonstrating high durability with a 72.6 % removal rate after five cycles, while post-adsorption characterization and leaching tests confirmed effective internal adsorption and minimal environmental risk, ultimately proving it to be an efficient and environmentally safe adsorbent. Overall, this article provides scientific support for the reuse of SMS to prepare BC for the remediation of pesticide pollution.

Funding information

This work was supported by the scientific and technological innovation capacity building project of BAAFS (KJCX20251007), the excellent youth science foundation of scientific and technological innovation capacity building project of BAAFS (YKPY2025003), and the National Natural Science Foundation of China [No.42107002].

CRediT authorship contribution statement

Yuhang Sun: Writing – original draft, Methodology, Formal analysis, Data curation. **Ping Han:** Validation, Investigation, Funding acquisition, Conceptualization. **Jing Li:** Validation, Software, Investigation. **Qi Gao:** Resources. **Mingyu Zhao:** Software. **Kai Wang:** Visualization. **Zhan Wang:** Resources. **Ercheng Zhao:** Resources. **Hongtao Zou:** Writing – review & editing, Supervision, Investigation, Conceptualization. **Junxue Wu:** Writing – review & editing, Supervision, Project administration, Funding acquisition, Conceptualization.

Declaration of competing interest

The authors declare that they have no known competing financial interests or personal relationships that could have appeared to influence the work reported in this paper.

Acknowledgement

This work was supported by the scientific and technological innovation capacity building project of BAAFS (KJCX20251007), the excellent youth science foundation of scientific and technological innovation capacity building project of BAAFS (YKPY2025003), and the National

Natural Science Foundation of China [42107002]. We thank Edible Fungi Lab in Institute of Plant Protection, Beijing Academy of Agriculture and Forestry Science for providing the SMSs in the experiments.

Supplementary materials

Supplementary material associated with this article can be found, in the online version, at doi:10.1016/j.hazadv.2025.100951.

Data availability

Data will be made available on request.

References

Ahmad, M., Lee, S.S., Dou, X., Mohan, D., Sung, J.K., Yang, J.E., Ok, Y.S., 2012. Effects of pyrolysis temperature on soybean stover- and peanut shell-derived biochar properties and TCE adsorption in water. Bioresour. Technol. 118, 536–544.

Ajala, O.J., Nwosu, F.O., Ahmed, R.K., 2018. Adsorption of atrazine from aqueous solution using unmodified and modified bentonite clays. Appl. Water. Sci. 8, 214.

Cao, B., Li, M., Zhang, T., Gong, T., Yang, T., Xi, B., Lu, H., Wang, Z., 2024. Dynamics and mechanisms of atrazine adsorption on biogas-residue biochar with citric acid modification. Sep. Purif. Technol. 337, 126151.

Cao, Y., Jiang, S., Zhang, Y., Xu, J., Qiu, L., Wang, L., 2021. Investigation into adsorption characteristics and mechanism of atrazine on nano-MgO modified fallen leaf biochar. J. Environ. Chem. Eng. 9 (4), 105727.

Chang, J., Fang, W., Chen, L., Zhang, P., Zhang, G., Zhang, H., Liang, J., Wang, Q., Ma, W., 2022. Toxicological effects, environmental behaviors and remediation technologies of herbicide atrazine in soil and sediment: a comprehensive review. Chemosphere 307 (3), 136006.

Chen, A., Wang, H., Zhan, X., Gong, K., Xie, W., Liang, W., Zhang, W., Peng, C., 2024a. Applications and synergistic degradation mechanisms of nZVI-modified biochar for the remediation of organic polluted soil and water: a review. Sci. Total. Environ. 911, 168548.

Chen, B., Zhou, D., Zhu, L., 2008. Transitional adsorption and partition of nonpolar and polar aromatic contaminants by biochars of pine needles with different pyrolytic temperatures. Environ. Sci. Technol. 42, 5137–5143.

Chen, L., Hu, J., Wang, H., He, Y., Deng, Q., Wu, F., 2024b. Predicting Cd(II) adsorption capacity of biochar materials using typical machine learning models for effective remediation of aquatic environments. Sci. Total. Environ. 944, 173955.

Chen, Y., Hassan, M., Nuruzzaman, M., Zhang, H., Naidu, R., Liu, Y., Wang, L., 2023. Iron-modified biochar derived from sugarcane bagasse for adequate removal of aqueous imidacloprid: sorption mechanism study. Environ. Sci. Pollut. R 30, 4754–4768.

Chun, Y., Sheng, G.Y., Chiou, C.T., 2004. Xing B. Compositions and sorptive properties of crop residue-derived chars. Environ. Sci. Technol. 38, 4649–4655.

Cui, Q., Zhang, M., Chen, M., Yang, C., Song, C., Sun, J., Yan, S., 2024. Comparative studies of sulfadiazine sodium degradation performance and mechanisms in the systems of persulfate with and without activation. Chem. Eng. J. 483, 149356.

Dong, X., Chu, Y., Tong, Z., Sun, M., Meng, D., Yi, X., Gao, T., Wang, M., Duan, J., 2024. Mechanisms of adsorption and functionalization of biochar for pesticides: a review. Ecotox. Environ. Safe 272, 116019.

Galan, I., Glasser, F.P., Andrade, C., 2013. Calcium carbonate decomposition. J. Therm. Anal. Calorim. 111, 1197–1202.

Gao, Z., Dai, Z., Wang, R., Li, Y., 2023. Adsorption kinetics and mechanism of atrazine on iron-modified algal residue biochar in the presence of soil. Environ. Sci. Pollut. R 30, 70506–70518.

Ghose, A., Mitra, S., 2022. Spent waste from edible mushrooms offers innovative strategies for the remediation of persistent organic micropollutants: a review. Environ. Pollut. 305, 119285.

Guo, Y., Song, S., Gao, Q., Yan, D., Rong, C., Qin, W., Liu, Y., Wang, S., 2022. Progress in resource utilization of edible fungus residue. J. Edible Fungi 29, 103–114.

Han, Z., Jiang, Q., Pei, Y., Zhao, C., Li, J., Dong, H., Cheng, Z., 2023. Type-effects of multiple waste-sourced biochar feedstocks on methylene blue adsorption. New. J. Chem. 47, 15057–15065.

Hawryluk-Sidoruk, M., Raczkiewicz, M., Krasucka, P., Duan, W., Masek, O., Zarzycki, R., Kobylecki, R., Pan, B., Oleszczuk, P., 2024. Effect of biochar chemical modification (acid, base and hydrogen peroxide) on contaminants content depending on feedstock and pyrolysis conditions. Chem. Eng. J. 481, 148329.

He, H., Liu, Y., You, S., Liu, J., Xiao, H., Tu, Z., 2019. A review on recent treatment technology for herbicide atrazine in contaminated environment. Int. J. Env. Res. Pub. He. 16 (24), 5129.

He, J., Li, J., Gao, Y., He, X., Hao, G., 2023. Nano-based smart formulations: a potential solution to the hazardous effects of pesticide on the environment. J. Hazard. Mater. 456, 131599.

Hu, Y., Jiang, Z., Hou, A., Wang, X., Zhou, Z., Qin, B., Cao, B., Zhang, Y., 2023. Impact of atrazine on soil microbial properties: a meta-analysis. Environ. Pollut. 323, 121337.

Ji, L., Wan, Y., Zheng, S., Zhu, D., 2011. Adsorption of tetracycline and sulfamethoxazole on crop residue-derived ashes: implication for the relative importance of black carbon to soil sorption. Environ. Sci. Technol. 45, 5580–5586.

Jin, J., Kang, M., Sun, K., Pan, Z., Wu, F., Xing, B., 2016. Properties of biochar-amended soils and their sorption of imidacloprid, isoproturon, and atrazine. Sci. Total. Environ. 550, 504–513.

Jing, X., Wang, Y., Liu, W., Wang, Y., Jiang, H., 2014. Enhanced adsorption performance of tetracycline in aqueous solutions by methanol-modified biochar. Chem. Eng. J. 248, 168–174.

Lattao, C., Cao, X., Mao, J., Schmidt-Rohr, K., Pignatello, J.J., 2014. Influence of molecular structure and adsorbent properties on sorption of organic compounds to a temperature series of wood chars. Environ. Sci. Technol. 48, 4790–4798.

Leite Vieira, R.A., Pickler, T.B., Mena Segato, T.C., Jozala, A.F., Grotto, D., 2022. Biochar from fungiculture waste for adsorption of endocrine disruptors in water. Sci. Rep. 12, 6507.

Li, R., Shen, X., Zhang, J., Jiang, Q., Wang, L., Zhang, Y., 2024. Tailoring biochar supported iron nanoparticles to activate persulfate for atrazine degradation in soil. J. Environ. Chem. Eng. 12 (2), 111967.

Li, X., Jiang, Y., Chen, T., Zhao, P., Niu, S., Yuan, M., Ma, X., 2023. Adsorption of norfloxacin from wastewater by biochar with different substrates. Environ. Geochem. Hlth. 45, 3331–3344.

Li, Y., Shang, H., Cao, Y., Yang, C., Feng, Y., Yu, Y., 2022. Quantification of adsorption mechanisms distribution of sulfamethoxazole onto biochar by competition relationship in a wide pH range. J. Environ. Chem. Eng. 10 (6), 108755.

Liang, Y., Tao, R., Zhao, B., Meng, Z., Cheng, Y., Yang, F., Lei, H., Kong, L., 2024. Roles of iron and manganese in bimetallic biochar composites for efficient persulfate activation and atrazine removal. Biochar. 6 (1), 41.

Lima, J.Z., Ogura, A.P., Silva, L.C.M.D., Nauerth, I.M.R., Rodrigues, V.G.S., Espindola, E. L.G., Marques, J.P, 2022. Biochar-pesticides interactions: an overview and applications of wood feedstock for atrazine contamination. J. Environ. Chem. Eng. 10 (5), 108192.

Liu, Y., Yao, L., Hu, B., Li, T., Tian, H., 2023. Adsorption behavior and residue degradation of triazine herbicides in soil amended with rice straw biochar. Agricult.-Basel 13 (7), 1282.

Liu, Y., Yuan, Y., Wang, Z., Yuan, W., Liu, L., Wang, T., Xie, X., 2022. Removal of ofloxacin from water by natural ilmenite-biochar composite: a study on the synergistic adsorption mechanism of multiple effects. Bioresour. Technol. 363, 127938.

Lou, Z., Wang, Q., Sun, W., Liu, J., Yan, H., Han, H., Bian, H., Li, Y., 2022. Regulating lignin content to obtain excellent bamboo-derived electromagnetic wave absorber with thermal stability. Chem. Eng. J. 430 (4), 133178.

Mohammed, N.A.S., Abu-Zurayk, R.A., Hamadneh, I., Al-Dujaili, H., 2018. Phenol adsorption on biochar prepared from the pine fruit shells: equilibrium, kinetic and thermodynamics studies. J. Environ. Manage 226, 377–385.

Peng, H., Li, H., Li, B., Zhou, Y., Wen, J., Zheng, X., 2023. $CuInS_2$-MgO/S-doped biochar heterojunction for the efficient adsorption-photocatalytic elimination of cationic dye. Chem. Phys. Lett. 832, 140862.

Raluca, C.S.I., van Staden, J.F., Stefan-van Staden, R.I, 2023. Minireview - recent developments in electrochemical detection of atrazine. Anal. Lett. 56, 847–869.

Sanchez, V., Francisco, Lopez-Bellido J, Rodrigo, M.A., Rodriguez, L., 2019. Enhancing the removal of atrazine from soils by electrokinetic-assisted phytoremediation using ryegrass (Lolium perenne L.). Chemosphere 232, 204–212.

Sanchez, V., Lopez-Bellido, F.J., Rodrig, M.A., Fernandez, F.J., Rodriguez, L., 2020. A mesocosm study of electrokinetic-assisted phytoremediation of atrazine-polluted soils. Sep. Purif. Technol. 233, 116044.

Sewu, D.D., Boakye, P., Jung, H., Woo, S.H., 2017. Synergistic dye adsorption by biochar from co-pyrolysis of spent mushroom substrate and Saccharina japonica. Bioresour. Technol. 244, 1142–1149.

Singh, R.P., Ahsan, M., Mishra, D., Pandey, V., Anupama, Yadav A, Khare, P., 2022. Ameliorative effects of biochar on persistency, dissipation, and toxicity of atrazine in three contrasting soils. J. Environ. Manage 303, 114146.

Shi, Q., Zhang, X., Shen, B., Ren, K., Wang, Y., Luo, J., 2021. Enhanced elemental mercury removal via chlorine-based hierarchically porous biochar with $CaCO_3$ as template. Chem. Eng. J. 406, 126828.

Soltysova, N., Derco, J., Horna, A., 2023. Kinetic study of the ozonation of atrazine. Chem. Biochem. Eng. Q. 37, 203–213.

Song, L., Cheng, H., Liu, C., Ji, R., Yao, S., Cao, H., Li, Y., Bian, Y., Jiang, X., Cwielag-Piasecka, I., Song, Y., 2024. Oyster shell facilitates the green production of nitrogen-doped porous biochar from macroalgae: a case study for removing atrazine from water. Biochar. 6 (1), 76.

Suo, F., You, X., Ma, Y., Li, Y., 2019. Rapid removal of triazine pesticides by P doped biochar and the adsorption mechanism. Chemosphere 235, 918–925.

Tan, G., Sun, W., Xu, Y., Wang, H., Xu, N., 2016. Sorption of mercury (II) and atrazine by biochar, modified biochars and biochar based activated carbon in aqueous solution. Bioresour. Technol. 211, 727–735.

Tao, Y., Han, S., Zhang, Q., Yang, Y., Shi, H., Akindolie, M., Jiao, Y., Qu, J., Jiang, Z., Han, W., Zhang, Y., 2020. Application of biochar with functional microorganisms for enhanced atrazine removal and phosphorus utilization. J. Clean. Prod. 257, 120535.

Tappin, A.D., Loughnane, J.P., McCarthy, A.J., Fitzsimons, M.F., 2012. Removal of atrazine from river waters by indigenous microorganisms. Environ. Chem. Lett. 10, 89–96.

Turan, N.B., Zaman, B.T., Chormey, D.S., Engin, G., Bakirdere, S., 2022. Atrazine: from detection to remediation - a minireview. Anal. Lett. 55, 411–426.

van der Zalm, J., Zeng, L., Chen, A., 2023. Experimental and computational studies of photoelectrochemical degradation of atrazine by modified nanoporous titanium dioxide. Chemosphere 318, 137985.

Wang, J., Yuan, M., Cao, N., Zhu, J., Ji, J., Liu, D., Gao, R., Pang, S., Ma, Y., 2023. In situ boron-doped cellulose-based biochar for effective removal of neonicotinoids: adsorption mechanism and safety evaluation. Int. J. Biol. Macromol. 237, 124186.

Wang, J., Zhang, J., Ma, Y., Zheng, B., Zheng, Z., Zhao, Y., 2012. Degradation of atrazine in water by gamma-ray irradiation. Fresen. Environ. Bull. 21 (9A), 2778–2784.
Wang, P., Cao, J., Mao, L., Zhu, L., Zhang, Y., Zhang, L., Jiang, H., Zheng, Y., Liu, X., 2022a. Effect of H_3PO_4-modified biochar on the fate of atrazine and remediation of bacterial community in atrazine-contaminated soil. Sci. Total. Environ. 851 (2), 158278.
Wang, P., Liu, X., Yu, B., Wu, H., Xu, J., Dong, F., Zheng, Y., 2020. Characterization of peanut-shell biochar and the mechanisms underlying its sorption for atrazine and nicosulfuron in aqueous solution. Sci. Total. Environ. 702, 134767.
Wang, P., Stenrod, M., Wang, L., Yuan, S., Mao, L., Zhu, L., Zhang, L., Zhang, Y., Jiang, H., Zheng, Y., Liu, X., 2022b. Characterization of montmorillonite-biochar composite and its application in the removal of atrazine in aqueous solution and soil. Front. Env. Sci. 10, 888252.
Wang, W., Wang, P., Wu, C., Zhang, L., Mao, L., Zhu, L., Jiang, H., Zheng, Y., Liu, X., 2024. Adsorption of acetochlor-contaminated water systems using novel P-doped biochar: effects, application, and mechanism. Chemosphere 350, 141027.
Wang, Y., Chen, Y., Wang, L., Mo, Y., Lin, X., Gao, S., Chen, M., 2025. Efficient removal of atrazine in wastewater by washed peanut shells biochar: adsorption behavior and biodegradation. Process Biochem. 15, 22–34.
Wang, X., Li, X., Liu, G., He, Y., Chen, C., Liu, X., Li, G., Gu, Y., Zhao, Y., 2019. Mixed heavy metal removal from wastewater by using discarded mushroom-stick biochar: adsorption properties and mechanisms. Environ. Sci.-proc. Imp. 21, 584–592.
Yasar, M., 2024. Synthetic studies of zinc-doped cadmium aluminum ferrite for the photocatalytic degradation of atrazine. React. Kinet. Mech. Cat. 137, 2469–2486.
Yavari, S., Malakahmad, A., Sapari, N.B., 2015. Biochar efficiency in pesticides sorption as a function of production variables-a review. Environ. Sci. Pollut. R 22, 13824–13841.
Zhang, B., Zhang, J., Wang, Y., Qu, J., Jiang, Z., Zhang, X., Tao, Y., Wang, Y., Kang, Z., Han, S., Zhang, J., Zhang, Y., 2024. Biodegradation of atrazine with biochar-mediated functional bacterial biofilm: construction, characterization and mechanisms. J. Hazard. Mater. 465, 133237.
Zhang, G., Zhang, Q., Sun, K., Liu, X., Zheng, W., Zhao, Y., 2011. Sorption of simazine to corn straw biochars prepared at different pyrolytic temperatures. Environ. Pollut. 159, 2594–2601.
Zhang, P., Sun, H., Ren, C., Min, L., Zhang, H., 2018. Sorption mechanisms of neonicotinoids on biochars and the impact of deashing treatments on biochar structure and neonicotinoids sorption. Environ. Pollut. 234, 812–820.
Zhang, T., Yu, H., Han, Z., Xu, S., Dong, Z., Zhou, K., Zhang, S., Cheng, Z., 2023a. Remediation of atrazine in environment by persulfate activation via N/B co-doped Si-rich biochar: performance, mechanisms, degradation pathways and phytotoxicity. Chem. Eng. J. 477, 147131.
Zhang, Y., Zhang, H., Zhang, A., Heroux, P., Sun, Z., Liu, Y., 2023b. Remediation of atrazine-polluted soil using dielectric barrier discharge plasma and biochar sequential batch experimental technology. Chem. Eng. J. 458, 141406.
Zheng, D., Wu, M., Zheng, E., Wang, Y., Feng, C., Zou, J., Juan, M., Bai, X., Wang, T., Shi, Y., 2022. Adsorption and oxidation of ciprofloxacin by a novel layered double hydroxides modified sludge biochar. J. Colloid. Interf. Sci. 625, 596–605.